

Turbulent Boundary Layer Control Using Wall Information

Gerardo E. Colmenero* and David B. Goldstein†
 Center for Aeromechanics Research
 Department of Aerospace Engineering
 The University of Texas at Austin
 Austin, TX 78712

Flow control may be achieved by using Micro Electro-Mechanical Systems (MEMS) to alter the fine scale flow structures within a boundary layer. In this study, a direct numerical simulation of slot jet MEMS in a turbulent channel flow is used to investigate flow control. We report on results of an array of discrete wall-normal actuators coupled with a control algorithm that uses wall information upstream of the jets to sense oncoming streamwise vortices. These vortices are a key phenomenon in the development and regeneration of turbulent flow and are therefore targeted to provide drag reduction over a channel wall. Preliminary results show that detection of a spanwise shear gradient at the channel surface provides an effective detection scheme as a drag reduction of 3.0% \pm 2.1% is achieved using an actuation strength such that in the slot exit plane $v_{rms} \approx 0.28u^*$. The total control area of the current array of actuators is equivalent to approximately 15% of the total wetted surface suggesting a larger reduction may be achieved by the addition of more actuators.

Nomenclature

$C_{deflection}$	=	membrane deflection scaling factor
h	=	channel half-height
ΔL	=	streamwise resolution
L	=	channel length
l^*	=	wall units or viscous length scale, ν/u^*
P_{amp}	=	gain constant of the actuator response
P	=	Pressure
$Re_{channel}$	=	centerline Reynolds number, $u_{cl}h/\nu$
R^*	=	turbulent Reynolds number, u^*h/ν
Δt	=	time delay constant, number of iterations
dt	=	time step
T	=	total flow duration
t^*	=	viscous time scale, l^*/u^*
u, v, w	=	velocity in streamwise, normal and spanwise directions
u_{cl}	=	channel centerline mean velocity
u^*	=	friction velocity, $(\tau_w/\rho)^{1/2}$
ΔW	=	spanwise resolution
W	=	channel width
x, y, z	=	streamwise, normal and spanwise directions
x^+, y^+, z^+	=	streamwise, normal and spanwise directions in wall units, x/l^*
μ	=	absolute viscosity
ν	=	kinematic viscosity
ρ	=	density
τ_w	=	wall shear stress on unmanipulated wall, $\Delta u/\Delta y$
$\omega_x, \omega_y, \omega_z$	=	streamwise, normal and spanwise vorticity components

* Graduate Research Assistant

† Associate Professor

I. Introduction

A turbulent boundary layer is characterized by coherent vortical structures that arise, evolve and decay in a quasi-periodic fashion. The structures, which are dominant in the near-wall region, occupy only 25% of this region but are responsible for approximately 50% of the total turbulence production.¹ Hence, the goal of many researchers and the present research is to actively weaken the coherent structures in the near-wall region to achieve drag reductions over a channel wall. There exist three regions in boundary layer flow that can be categorized by how certain terms in the turbulent energy equation compare, specifically how the rate of turbulent energy production compares to its dissipation. The outer region of the boundary layer can be characterized as a place where turbulent energy dissipation is greater than the rate of production.² This is due to the fact that in this region turbulent shear, associated with eddy viscosity and turbulence dissipation, is dominant over the molecular viscosity effects, which is associated with viscous shear and the no-slip boundary condition of the wall.³ In the logarithmic region of a boundary layer, the energy dissipation and the rate of energy production are of equal magnitude and in general nothing happens in this region except the passing of structures from one region to another.² The third region closest to the wall, $y^+ < 100$, consists of the viscous sub-layer through the inner portion of the log layer. Here the rate of production is dominant over dissipation. It is the manipulation of this inner region that interests researchers since it provides the greatest potential for reduction of turbulent energy production. Furthermore, reducing the rate of production also reduces the passage of energy away from the wall which helps to maintain turbulence. Consequently, for wall-bounded flows, it is suggested² that a quasi-periodic turbulence cycle exists in the near-wall region ($20 < y^+ < 60$) and it is independent of flow in the interior of the channel. Therefore, understanding of the physics of the regeneration cycle in this region is important and this cycle is briefly described.

Jimenez et al.² suggests that the near-wall region is dominated by streamwise velocity streaks superimposed on the mean shear, where the mean shear is maintained by the no-slip boundary condition of the wall. It is well known that streaks can be very long, $x^+ \approx 1000$, have a width of 20-40 δ^* , and have an average spanwise spacing of $z^+ \approx 100$.⁴ In addition to streaks, quasi-streamwise vortices dominate the near-wall region; however, because the vortices are not aligned parallel to the wall they only remain in this region for approximately $x^+ \approx 200$.² Therefore due to the shorter length of the quasi-streamwise vortices it seems that several vortices can be associated with each velocity streak. This suggests that the physical vortex/streak interaction is crucial for the life of both structures; and in general, it suggests there are more vortices in the near-wall region than there are velocity streaks. The explanation of how the streaks are created is roughly as follows; as the structures convect downstream, the quasi-streamwise vortices tend to pump high momentum fluid from the core region of the channel towards the wall creating sweep events while also pumping low momentum fluid from the near-wall region towards the center of the channel creating an ejection event. The sweep and ejection events result in the alternating streaks of streamwise velocity. Furthermore, the generation of the quasi-streamwise vortices results from inflectional instabilities introduced by the streaks which affect the velocity profiles.²

Consequently, the mixing of the high and low momentum fluid in the channel, resulting primarily from the sweep and ejection events, helps to create a fuller mean velocity profile characteristic of a turbulent channel flow. As a result, the steeper velocity gradient near the channel walls results in a much higher viscous drag than would laminar flow at the same bulk channel velocity.⁵ Therefore it is argued that the weakening of the streamwise vortices in the region $20 < y^+ < 60$ may achieve reductions in skin-friction drag. This effect has been observed with passive devices such as riblets. In the case of passive devices, the streamwise vortices are weakened by increasing the spanwise friction above the riblet crests⁶ and by the restriction of the vortices such that only a limited area of the riblet is exposed to the sweep event that the vortices induce.⁷ However, the objective of this project is the active control of the near-wall region to accomplish drag reduction. In contrast to passive devices, active control weakens the coherent vortical structures through more direct mechanisms.

Active control of the turbulent boundary layer has been applied using numerous techniques. The overall objective is the use of small sensors and actuators to provide effective control based on easily measurable flow quantities. The progression of research in this area started with physical, intuitive arguments of the boundary layer features but then shifted towards the use of parametric approaches with the end goal of weakening of the near-wall coherent vortical structures and thereby reducing drag. A brief summary follows describing the numerical and experimental work that has led to the development of the current simulation of turbulent boundary layer control.

A. Numerical/ Experimental Progress in Turbulent Boundary Layer Active Control

Choi et al.⁸ uses a physical approach to create a numerical opposition control method. In this method, depicted in figure 1, the vertical motion of the near-wall turbulent flow, which is thought of as resulting from the quasi-

streamwise vorticity, is sensed at $y^+ \approx 15$ and countered by an equal but opposite blowing/suction distribution velocity on the wall.

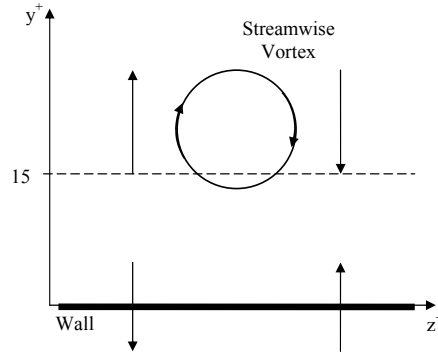


Figure 1. Choi et al.⁸ opposition control scheme to weaken streamwise vortices in the near-wall region of turbulent channel flow. Vertical motion induced by the streamwise vortex is sensed, say, at $y^+ \approx 15$. An opposing blowing/suction velocity distribution is applied on the channel wall.

The technique results in a 25% drag reduction. However, one major drawback of the method is that it requires knowledge of the flow variables within the flow domain. Also, the opposition control is instantaneously applied at every point along the wall throughout the entire channel domain. These drawbacks make the method impractical to implement physically. The work, however, sparked others to develop more practical methods for detection and actuation.

Koumoutsakos et al.⁹ sought a numerical feedback control algorithm that uses flow information detected at the wall. The actuating mechanism of this approach is effectively the blowing/suction velocity distribution at the wall, similar to the method of Ref. 8. In order to maintain a reasonable level of actuation, actuation strength is limited to a threshold value of 5-15% of the mean bulk velocity. The control scheme is based on the manipulation of the spanwise and streamwise vorticity flux components obtained by measuring the instantaneous pressure at the wall and calculating its gradient. The equations relating the two quantities, shown below, were derived from the momentum equation evaluated at the wall.

$$v \left(\frac{\partial \omega_x}{\partial y} \right)_{\text{wall}} = \frac{1}{\rho} \left(\frac{\partial P}{\partial z} \right)_{\text{wall}}, \quad -v \left(\frac{\partial \omega_z}{\partial y} \right)_{\text{wall}} = \frac{1}{\rho} \left(\frac{\partial P}{\partial x} \right)_{\text{wall}}, \quad (1)$$

where P is the pressure and ω_x and ω_z are the streamwise and spanwise vorticity components. Results using this approach show up to 40% drag reduction for low Reynolds number turbulent channel flow.

Kang et al.⁷ and Carlson et al.¹⁰ sought a different actuation mechanism for suppressing the strength of the near-wall streamwise vortices. In Ref. 10 a Gaussian shaped actuator approximately $12l^*$ high is installed on the wall. Carlson et al.⁸ show that raising the actuator below a high-speed streak decreased skin-friction drag by allowing the associated low-speed fluid region to expand. In comparison, the approach of Ref. 7 reduces skin-friction drag by locally deforming the wall with basic coordinate transformations, thereby inducing a blowing/suction velocity distribution based on two previously imposed feedback control strategies.^{8,11} Results show that for a channel flow at $R^* = 140$, 13-17% drag reduction is obtained using the active wall motions. This reduction is smaller than the reductions of Ref. 8 and 11 possibly due to the limitation of the height of the wall deformations in the study.⁷ In addition, the results show that active control using wall deformations shifts the mean velocity away from the wall within the logarithmic region and reduces the turbulence intensities; this upward shift appears common in turbulent flows with skin-friction drag reduction.⁷ An interesting observation is that the root-mean-squared amplitudes of the wall deformations are approximately $3.2l^*$ and resemble riblets because the wall deformations extend in the streamwise direction. However, Kang et al.⁷ found that the mechanism resulting in a reduction of skin-friction drag is due to the direct suppression of the coherent near-wall structures through induced blowing/suction at the wall and not by the passive mechanisms characterized by riblets.

Endo et al.¹² developed a numerical feedback control method with an array of sinusoidal deformable wall actuators roughly $172l^*$ by $60l^*$ to minimize the near-wall coherent structures. When using the opposition control

scheme similar to Ref. 8 to determine the local wall velocity, the drag is decreased by $\sim 12\%$ with a wall deformation magnitude on the order of $1l^*$. In addition, a second scheme was developed using only wall information. Endo et al.¹² describes the spanwise meandering of the near-wall streamwise streaks as playing an important role in the quasi-cyclic turbulence regeneration process, and he uses the meandering of the streaks to argue that quasi-streamwise vortices accompanied with the meandering streaks can be detected by measuring the streamwise and spanwise gradient of the wall shear stresses. They conclude that by using only wall information they can actuate on quasi-streamwise vortices $50l^*$ downstream from the wall sensors. Through the active wall deformation of arrayed sensors and actuators a 10% drag reduction can be achieved.

In addition to the above applications, research on the control of turbulent boundary layers has made use of control theory to examine the control algorithms. Lee et al.¹¹ developed a sub-optimal feedback control law that requires pressure or shear stress information only at the wall. Using the blowing/suction actuation of Ref. 8, the numerical method was applied using as the detection variables the local gradients of pressure and shear stress in a turbulent channel flow at $R^* = 110$ resulting in a 16-22% reduction in skin-friction drag. The ability to measure pressure gradients at the wall resulted from the observation of Lee et al.¹¹ that opposition control of the wall-normal velocity component of a streamwise vortex near the wall increases the pressure gradient in the spanwise direction directly below a streamwise vortex structure (see Fig. 2).

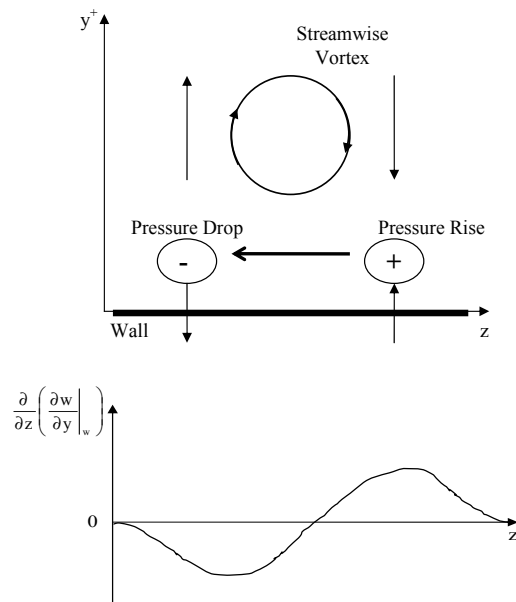


Figure 2. A key observation by Lee et al.¹¹ is the measurement of a spanwise pressure gradient at the wall resulting from the interaction of a vortex near the wall. This suggests a spanwise increase in pressure gradient directly below streamwise vortices. In addition, the spanwise gradient of the spanwise wall shear stress (profile shown above) can be used to detect a streamwise vortex.

However, of the two detection quantities used by Lee et al.¹¹, they found that the spanwise derivative of the spanwise shear at the wall is a slightly better quantity to use as a control input as it results in a 22% reduction in skin-friction drag.

Lee et al.¹³ make use of a neural network based on the spanwise wall shear stresses to activate the blowing/suction velocity distribution at the wall, achieving a 20% reduction of skin-friction. The numerical control scheme detects edges of local high-shear stress regions, which are elongated in the streamwise direction, by measuring the spanwise variation of the spanwise shear stress. They investigate how wall shear stresses correlate to wall actuations and make use of a neural network to approximate the correlation which then predicts the optimal wall actuation. They find that the detection of the spanwise shear stress at several points across a spanwise distance of $z^+ = 90$ is enough to achieve good performance of the control algorithm. Furthermore, the correlations suggest that the root-mean-squared value of the actuation should be approximately $0.15u^*$ for suppression of the near-wall streamwise vortices.

Experimental investigations into the active control of the near-wall turbulent boundary layer also play an important role in finding practical methods of weakening the near-wall coherent structures that produce turbulence. However, experiments on turbulent boundary layer control are difficult to achieve due to the small length and time scales that characterize turbulent flow, making the design and fabrication of sensors and actuators very difficult.¹⁴ Rathnasingham and Breuer¹⁴ investigate the active control of the near-wall turbulent boundary layer by using the key assumption that the dynamics of the large-scale coherent structures can be described as a linear process for a short period of time. The assumption is based on the observation that the mean shear of the near-wall turbulent flow will dominate during the short time it takes for the flow perturbations to evolve.¹⁵ In addition, it is important to note that the assumption holds only for the time it takes a structure to convect from a sensor to an actuator, and does not imply that turbulence production is a linear mechanism.¹⁴ Using an array of upstream flush-mounted sensors and flush-mounted resonant membrane-type actuators, a series of experimental observations of the boundary layer provide the optimal transfer functions to predict the downstream characteristics of the streamwise velocity fluctuations. This process predicted, in contrast to the numerical correlations of Lee et al.¹³, that the control jet amplitude is approximately three times stronger resulting in an optimal range with root-mean-squared values of $0.45 - 0.55u^*$.¹ The difference in actuation strengths may be due to the observation that in Ref. 1 the actuators are discrete jets that do not cover the entire domain and therefore may need stronger actuations locally while the actuation mechanism of Ref. 13 is an instantaneous blowing/suction velocity distribution of the entire domain wall. In addition to finding the optimal transfer functions, the detection techniques were optimized to isolate the large-scale turbulent motion and improve the downstream correlations. Control results show a maximum reduction of streamwise velocity fluctuations of 30%, with the reduction spanning a region $100l^*$ downstream of the actuator, $50l^*$ in the spanwise direction, and $150l^*$ in the wall normal direction. Furthermore, results show wall pressure fluctuations were reduced by 15%, the local mean wall shear stresses were reduced by 7% and the bursting frequency, associated with sweep events, is reduced by up to 23%.¹⁴

Rebeck et al.¹⁶ experimentally investigates how the near-wall turbulence structure of the boundary layer is modified when opposition control is attempted with a piston-type actuator. The actuator produces a wall-normal jet to cancel the downwash of high-momentum fluid associated with a sweep event. The effectiveness of the control method is judged from the observed changes in the burst intensity of the near-wall events. It is found that the performance of the control is very sensitive to the phase lag between detection and actuation. Specifically, the investigation shows a similar magnitude of burst intensity reduction when the opposition control is applied slightly late. However, the effectiveness is significantly reduced when the jet is issued early.

Another experimental investigation by Lew et al.¹⁷ uses a linear array of MEMS surface shear stress sensors and a micro-machined pneumatic flap actuator for to eliminate streak-like regions of high shear stress before their natural dissipation occurs along the channel wall. Open-loop actuation tests show that over an actuation cycle a net reduction of surface shear stress results. It is also found that the reduction is proportional to the actuation amplitude in relation to the boundary layer thickness.¹⁷ Furthermore, to ensure interaction with the coherent structure, the actuation amplitude of the flap was limited to $y^+ < 7$ which puts it just beyond the viscous sub-layer. In addition, they show that the high shear stress regions occupy approximately 40% of the surface area and contain approximately 70% of the total surface shear.

Jacobson et al.¹⁸ developed a piezoelectric cantilever flush-mounted with the wall to investigate active control of transitional and turbulent boundary layers. Actuation is applied by allowing a part of the flow surface to oscillate in and out of a cavity in the surface. The objective is to demonstrate control on steady and unsteady streamwise vortex disturbances in a laminar boundary layer, with the disturbances acting similar to eddies in the wall region of a turbulent boundary layer. The main idea is to draw fluid into the wall and pump it back out in a controlled manner in order to modify the near-wall flow. The piezoelectric actuator acts like a controllable vortex pair generator with no net mass flow through the boundary surface. The strength of the generated vortices is controlled by the amplitude of the actuator. Results show that the vortices are localized over the actuator and decay quickly downstream while the associated high- and low-speed streaks remain far downstream of the actuator.¹⁸ Other interesting results of the investigation are the dimensional scales found necessary to implement active control successfully. Jacobson et al.¹⁸ suggests the spanwise dimension of the control module should be of order $20l^*$ and in the streamwise dimension of order $200l^*$, totaling a control area of $Ac^+ \approx 4000$.

This review has brought to light recent progress made in turbulent boundary layer control research. Now the goal is to use aspects of the successful control techniques discussed above to develop a practical control method using our current numerical scheme¹⁹ to best model a realistic simulation of turbulent flow control. The average length and time scales of the near-wall coherent phenomena appear well documented, as are appropriate detection methods and dimensions of a successful control algorithm. In particular, the results of Breuer et al.¹ and Lee et al.¹³ suggest that the root-mean-squared control jet amplitude should be in the range of $0.15-0.55u^*$, with perhaps a tendency toward

the stronger actuations if modeling discrete actuators versus using a uniform distribution of wall-normal velocity on the domain wall. In addition, a control algorithm should closely model the control modules on the dimensions of those in Rathnasingham et al.¹⁴, where the sensors used are hot-wires aligned in the streamwise direction and the resonant membrane-type actuators are narrow in the spanwise dimension ($\sim 10l^*$) and long in the streamwise dimension ($\sim 150l^*$). These dimensions are roughly the same as those suggested by Jacobson et al.¹⁸ Moreover, the findings of Rathnasingham et al.¹⁴ suggest that the average convection speed of the large-scale structures of turbulent flow is approximately $u^+ = 10.7$. This allows a control algorithm to account for the time between the detection event upstream of the actuators and the actuation event imposed on the structures downstream. Finally, if the control algorithm requires flow variables measured at the wall only, a good detection scheme to model is that of Lee et al.¹¹ this scheme detects the spanwise derivative of the spanwise shear stress at the wall and has been shown to work successfully for Endo et al.¹²

B. Current Turbulent Boundary Layer Control Methodology

As described above, substantial reductions in drag can be achieved by wall-mounted actuators operating on the vortices or streaks to either stabilize the flow or reduce shear.²⁰ In order to do so, practical devices able to achieve fine flow control at the small scales near the surface need to be developed and their detailed interaction with a boundary layer needs to be studied. Therefore, we develop two control schemes shown together in Fig. 3; the first a feedback control algorithm based on the detection methodology of Lee et al.^{11,13} and another based on the experiments of Lew et al.¹⁷ In addition, we use an array of discrete wall-normal MEMS micro-actuators that detect wall information upstream of the jets to sense and act upon oncoming streamwise vortices.

Our early numerical studies²¹ have shown that when continuously operated in a turbulent boundary layer, small MEMS devices can substantially affect structures well beyond the buffer layer but such strong actuation was not found to decrease drag on the surface. Further studies with a single row of actuators²² show that the physics of an array of actuators differs considerably from the idealized case of uniform suction/blowing at the surface as in Ref. 5, 8. However, the research reviewed in the previous section hints at the potential of discrete actuators in achieving some form of flow control. Thus the goal of this study is to simulate a physically realistic method of turbulent boundary layer control. The use of wall information upstream of individual actuators to detect oncoming streamwise vortices modifies our previous velocity opposition control method in Ref. 22. In the previous approach, which is based on the opposition control method of Choi et al.⁸, the wall-normal velocity was sensed directly above each actuator slot along a plane $10.6l^*$ above the wall as shown in Fig. 4. An instantaneous response from the slot jets counteracted the detected wall-normal velocity. The objective of the current study is to compare the reduction in drag of that method²² with the more feasible method of upstream detection of wall information. It will also be interesting to see how the results of this current simulation will compare to those of Endo et al.¹² since the actuating mechanisms are similar; the main difference is our use of sub-surface sinusoidal membranes within cut out actuator slots. A brief discussion of the computational method and domain is followed by a detailed discussion of our results.

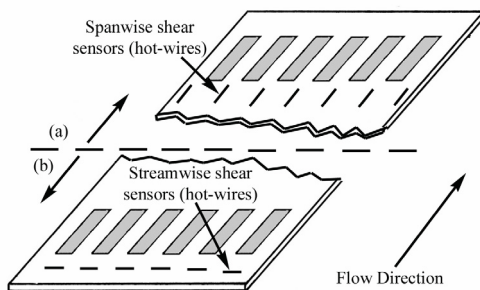


Figure 3. Schematic of the current detection schemes. Modeled as hot-wires approximately $2l^*$ above the surface; (a) detection of spanwise gradient of spanwise shear (based on Lee et al.^{11,13}); (b) detection of regions of high and low wall shear stress (based on Lew et al.¹⁷).

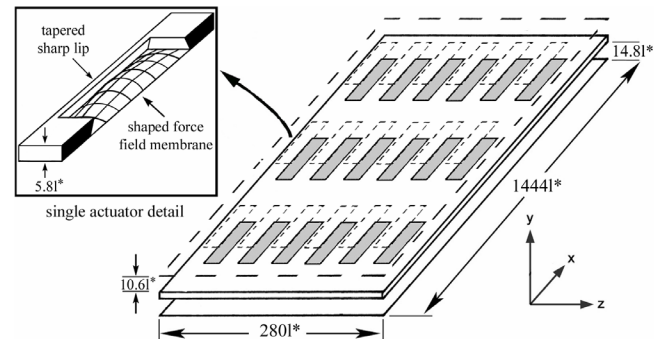


Figure 4. Schematic of manipulated surface with array of actuators and actuator detail. Sensing regions of Lee²² (based on the Choi⁸ approach) above each slot are indicated with dashed lines.

II. DNS Method and Computational Domain

The spectral method initially used by Kim et al.²³ expands the spatial variables of the incompressible Navier-Stokes equations with Fourier and Chebyshev polynomials. The equations are solved with a Chebyshev-tau method with cosine grid clustering in the wall-normal direction. Time stepping is done with an Adams-Bashforth scheme for the non-linear terms and Crank-Nicholson for the viscous terms. A localized force field similar to the one described by Goldstein et al.¹⁹ is used to simulate stationary and moving boundaries that make up the various parts of the actuators. Please refer to Ref. 21, 22, and 24 and related publications for more details and issues related to validation and convergence.

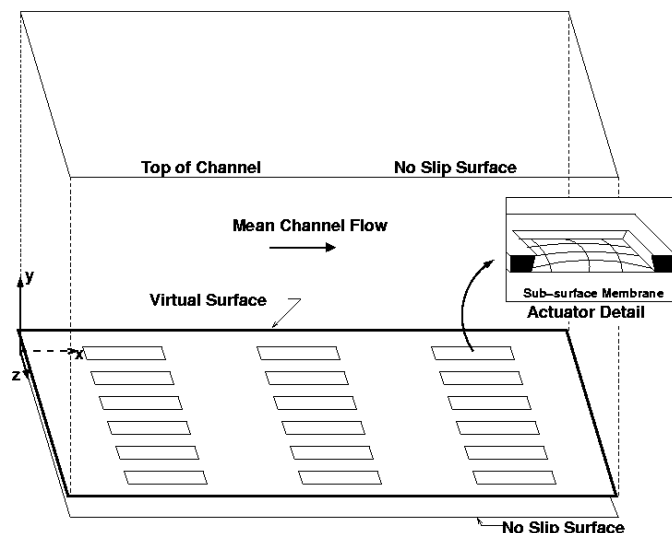


Figure 5. The full computational domain is shown including the no-slip channel boundary condition along the wall-normal axis. Also shown is the virtual surface created with the method of Goldstein et al.¹⁹ just above the bottom boundary. A close up of the actuator is shown including the sinusoidal sub-surface membrane that creates the actuator pumping/suction action.

The full computational domain, shown in Fig. 5, consists of a rectangular channel with mean flow in the x -direction. Flow is periodic in both the x and z directions while the horizontal top and bottom y -normal planes are defined as the channel boundaries. The discrete actuator (inset of Fig. 5), is configured to be similar to those being tested in Ref. 14 and 25. Individual rectangular holes are cut in a raised plate mounted above the lower boundary of the channel. The lips of each slot are tapered to be wider at the membrane location and narrower at the exit plane. The sharp lips are used to promote vortex separation²⁵ which was thought to be especially useful if modeling jet interactions with the turbulent boundary layer. The membranes are modeled flush at the bottom of each cutout to make up the driving mechanism of each actuator. Membrane deflection is scaled using a factor, $C_{deflection}$, to match the volumetric displacement of a piston-like motion. That is, a unit displacement input to the membrane results in a larger than unity peak deflection that produces that same amount of ejected fluid as the membrane undergoing a piston-like displacement of one unit. Additionally, while each slot has its own driving mechanism, all slots share a common subsurface cavity that supplies fluid for the pumping/suction action. For the domain in this study, $Re_{channel}$ was about 2,118 while R^* was about 116. For consistency, the friction velocity u^* , viscous length scale l^* and viscous time scale t^* were taken from the opposing top wall of the channel that contained no actuators. Those values were taken as constants and used throughout the study whenever friction properties were needed to normalize data or figures. With these parameters, the computational domain measured $280.2l^*$ in width and $1,443.7l^*$ in length. A summary of the relevant flow parameters for the turbulent channel flow is given in Table 1.

Table 1. Summary of relevant flow parameters for the turbulent channel flow.

<i>Quantity</i>	<i>Value</i>
Centerline Reynolds number - $Re_{channel}$	~ 2118
Turbulent Reynolds number - R^*	~ 116
Friction velocity - u^*	0.03007
Viscous length scale - l^*	0.00831
Viscous time scale - t^*	0.27635
Channel height - $2h$	$233.6l^*$
Channel length - L	$1,443.7l^*$
Channel width - W	$280.2l^*$
Streamwise resolution - ΔL	$\sim 7.5l^*$
Spanwise resolution - ΔW	$\sim 1.5l^*$
Time step - dt	0.0075
Number of grid points - x, y, z	128, 64, 128

III. Results and Discussion

A. Feedback Control Algorithm with Detection of $\partial/\partial z(\partial w/\partial y)|_{wall}$

1. Overview of Control Algorithm

In this section we discuss the results of the current detection methodology which is based on that of Lee et al.^{11,13} In particular, the spanwise gradient of the spanwise shear stress is used to detect the near-wall quasi-streamwise vortices upstream of an array of MEMS micro-actuators. Here we give detailed dimensional information of the control algorithm. Using the immersed boundary technique of Goldstein et al.¹⁹ we closely model the control module, i.e. the actuator and detection mechanism, of Rathnasingham et al.¹⁴ In their study, a pair of hot-wires aligned in the streamwise direction was placed upstream of the actuator to detect the spanwise wall shear stress. By differencing the pair signal, the derivative of the spanwise shear can be approximated. The spanwise spacing between hot-wires is equivalent to the characteristic streak width of $50l^*$. In the current control algorithm we model such hot-wires by detecting the spanwise component of velocity at two different points, approximately $2l^*$ above the wall and approximately $47l^*$ apart. Since the detection points are located deep in the viscous sub-layer, measuring the wall shear stress is simply a matter of detecting the velocity component of interest, in the current case it is the spanwise velocity component, and dividing by a constant wall-normal height ($2l^*$). Knowing the exact spanwise spacing of the detection points allows us to calculate an approximation of the spanwise gradient of the spanwise shear stress at the wall. A typical profile of this quantity is shown in Fig. 2 for a streamwise vortex. As shown in that schematic $\partial\tau_z/\partial z$ can be a clear indication of the presence of a streamwise vortex. The numerical approximation of the measured quantity used is given as:

$$\left. \frac{\partial}{\partial z} \left(\frac{\partial w}{\partial y} \right) \right|_{\text{approximated}} \cong \left[\frac{w_1}{\Delta y} - \frac{w_2}{\Delta y} \right] \cdot \frac{1}{\Delta z}; \quad \text{where } \Delta y = 2l^*, \Delta z = 47l^* \quad (2)$$

Multiplication by a gain constant, P_{amp} , of the $\partial\tau_z/\partial z|_{wall}$ and membrane deflection scaling factor yields the opposition blowing/suction magnitude of the actuators.

$$(v_{\text{blowing/suction}})_{\text{time=t}} = (P_{amp}) \cdot (C_{\text{deflection}}) \cdot \left[\frac{\partial}{\partial z} \left(\frac{\partial w}{\partial y} \right) \right]_{\text{approximated at time=t}-\Delta t} \quad (3)$$

The dimensions of the actuator, at the wall surface, are approximately $23l^*$ wide and $143l^*$ long which roughly models the $10l^*$ by $150l^*$ of Ref. 14. Furthermore, the current size of the control module follows that of Jacobson et al.¹⁸ which suggests control modules of order $20l^*$ wide and $200l^*$ in length. The current algorithm is extended into an array of 18 actuators each with a pair of upstream wall shear stress sensors to detect the oncoming streamwise

vortices. The array, as shown in Fig. 3-5, consists of three rows spaced evenly along the streamwise direction. Each row contains six actuators placed such that the actuators are aligned directly behind each other and have a pitch of approximately $47l^*$. The mean flow is periodic in the streamwise and spanwise directions. In addition, the total cut-out area covered by the array of actuators corresponds to 15% of the total surface. The time between the detection event upstream of the actuators and the actuation response is accounted for in the present control method. Using the findings of Rathnasingham et al.¹⁴, which suggest that the average convection speed of the large-scale turbulent structures is approximately $u^+ = 10.7$, and coupled with the finding that quasi-streamwise vortices were successfully detected $50l^*$ upstream of an actuation location by Endo et al.¹², the current detection points were placed approximately $53l^*$ upstream of the leading edge of the actuator. A delay time variable was introduced into the control algorithm to account for the convection time necessary for the detected vortical structure to reach the specified actuator. That time delay is parametrically examined below. A general summary of the control system as described above is shown as a schematic in Fig. 6.

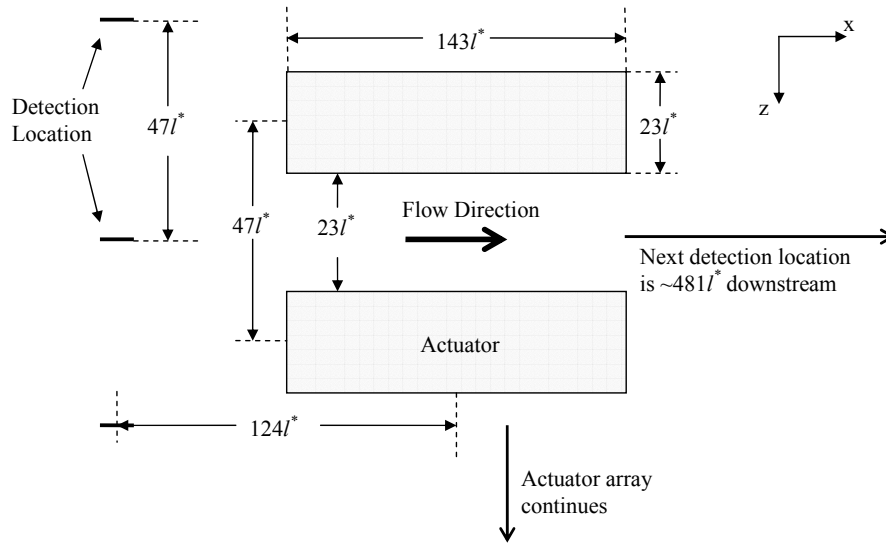


Figure 6. Summary of detection scheme including spatial dimensions for a portion of the controlled surface. Detection points (modeled as hot-wires aligned in the streamwise direction) are spaced to best sense a streamwise vortex. A time delay variable is introduced into the control algorithm to account for the time it takes a structure to convect the distance from the sensor to the actuator. Length and width of the actuator follow dimensions suggested in Ref. 14 and 18.

2. Optimal Signal Gain

A study was performed to determine the size of a gain constant, $Pamp$, used to determine the strength of the actuating mechanism based on Eq. 3. The results of Breuer et al.¹ and Lee et al.¹³ suggest that an actuation gain is applied such that the root-mean-squared control jet amplitude is in the range of $0.15-0.55u^*$. Since the current scheme models discrete actuators, we felt inclined toward the stronger end of this amplitude range. A brief parametric study of the $Pamp$ constant was performed to determine that the best case scenario, i.e. the case which resulted in the largest short-term drag reduction, was used in our long-term simulation run. Figure 7 displays the range of the actuator gains examined along with the number of time steps of delay. The figure shows the region of near-wall flow stability for various test cases. Stability was determined through the observation of the near-wall flow over the controlled surface during a series of short simulations. The tests showed that if $Pamp$ is set too large, above ~ 0.75 , the actuating membranes are forced too hard. This causes the near-wall flow instability as well as CFL failure in the more extreme cases. These gains are outside of the green shaded stable region of Fig. 7. As will be discussed shortly, it was found that where the root-mean-square of the control jet amplitude is approximately $0.28u^*$ the drag appeared minimized. This corresponds to a $Pamp = 0.5$, and as shown in Fig. 7, this value of gain is in the stable region for all values of time delay examined.

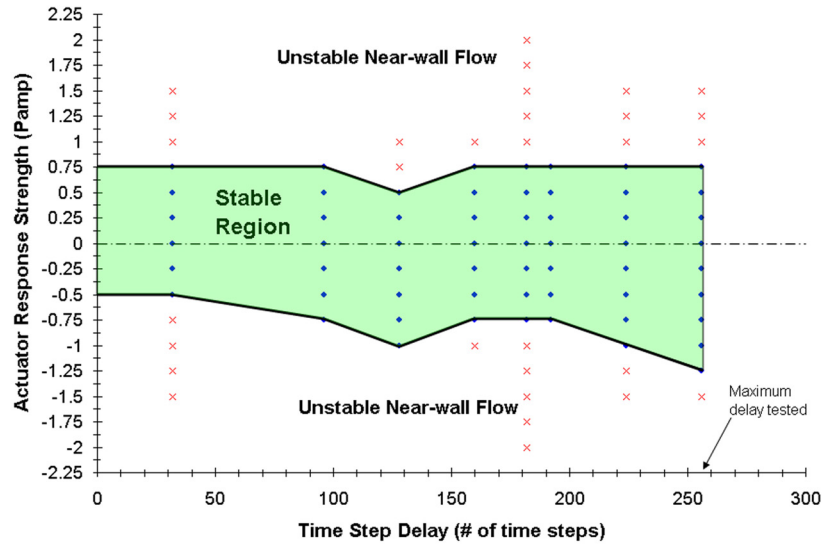


Figure 7. Stability plot of actuator gain constant, $Pamp$, and time delay, Δt , parametric study. Stability of the near-wall flow was determined through observation of the near-wall flow over the controlled surface during a short simulation. The stable region is shaded in green and blue dots represent stable test points. Red x's represent test points where the near-wall flow of the controlled surface was visually unstable.

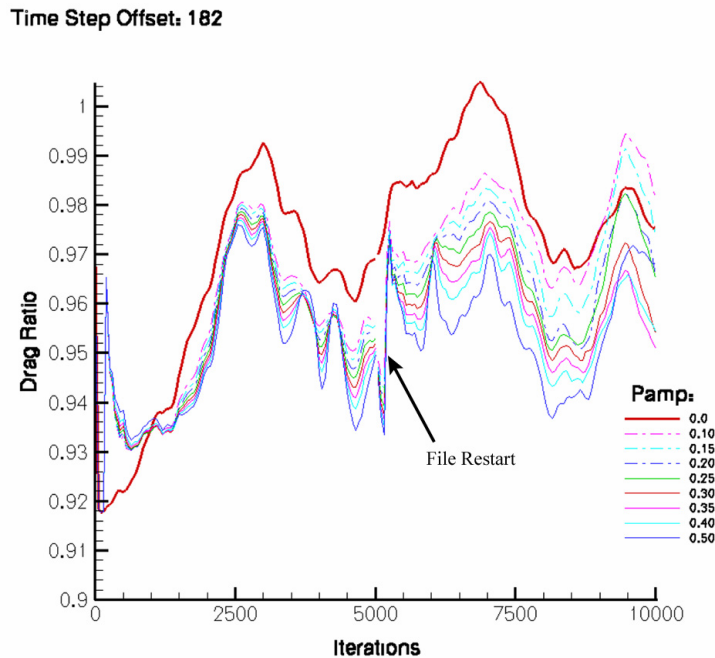


Figure 8. Drag trace of positive $Pamp$ values within the stable region of Fig. 7 with $\Delta t = 182$. The short run shows using a $Pamp = 0.5$ consistently results in the largest drag reduction. The glitches at iteration 1 and 5000 are due to simulation restart points that did not account for the final 182 time steps. Such glitches are corrected in the long-term simulations.

Figure 8 shows a series of drag traces for different gains compared to the inactive case of $Pamp = 0.0$. The drag ratio parameter is defined as the drag of the actuated surface divided by the drag of the opposing flat wall. A time delay of 182 time steps was imposed in the simulations. The traces show that a $Pamp = 0.5$ results in a large and consistent drag minimization throughout the simulation. In Fig 9a the drag traces are shown for the full range of positive gains examined in the parametric study. In Fig. 9b example drag traces using the negative $Pamp$ values are shown. In both Fig 9a and b, CFL failures result indicating the occurrence of flow instability for $Pamp$ values above 1.0. In Fig. 9b, note that drag *increases* are generally shown for the smaller magnitude (negative) $Pamp$ gains suggesting that a positive value is necessary. Based on such a parametric study, it was determined that $Pamp_{optimal} \approx 0.5$. In the sections that follow we compare inactive ($Pamp = 0.0$) control to the active case where our $Pamp$ is set to 0.5, unless otherwise stated.

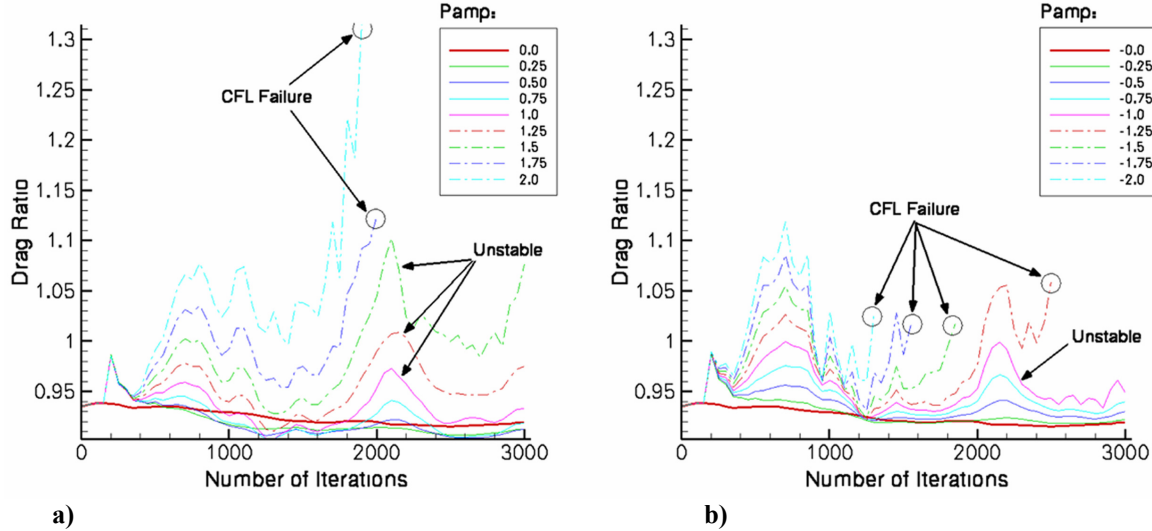


Figure 9. (a) Drag traces of entire range of positive $Pamp$ examined in parametric study at the particular case of $\Delta t = 182$. The traces support the observation of near-wall flow instabilities on the controlled surface for large $Pamp$ values. (b) Traces showing the negative $Pamp$ values. In general, no negative $Pamp$ resulted in a consistent drag reduction and most resulted in unstable near-wall flow thereby supporting the use of a positive $Pamp$ for the optimal drag reduction.

3. Optimal Time Delay

A brief parametric study is also performed to determine the optimal time delay, or lag, between the detection of the oncoming turbulent structure and the actuation of the sub-surface membrane. This is done by fixing the streamwise distance of the upstream sensors and varying the time delay variable, Δt .

It is found that the time delay variations of the study, oddly, have very little effect over a range of Δt $0.87 \rightarrow 6.95t^*$. In Fig. 10, the drag ratio of the inactive case is compared to that of the active case for various Δt . Note how changing the time delay shifts the data to the right, indicating a longer delay between detection and actuation events. This zoomed in portion of a short simulation supports the fact that, at least for the delays considered, a very small effect is observed. A possible explanation for the lack of a significant effect of Δt is that typical lengths of the velocity streaks can extend up to $1000t^*$ in the streamwise direction⁴ which corresponds to approximately $93t^*$ when assuming $u_c^+ = 10.7^{14}$ as the average streamwise convection speed of the large-scale turbulent structures. Since the range of the time delay variable used in this parametric study is short compared to the duration of an individual streak it is possible that the range examined is too small and results in no net effect. At first this seems to contradict the study of Rebbeck et al.¹⁶ where they find the control performance to be very sensitive to the phase lag between detection and actuation; however, in that study they detect bursting frequencies which are associated with sweep events. Sweep events are known to be much shorter in streamwise length, typically between $20-90t^*$, corresponding to a range of time delay of approximately $2-8t^*$. However, since our current method seeks to stabilize the near-wall flow with the detection of long low-speed streaks, time delay may have very little effect. As a result, we set $\Delta t = 182$ iterations (or approximately $5t^*$) which is equal to the convection time of a structure from the detection location to the actuator slot leading edge.

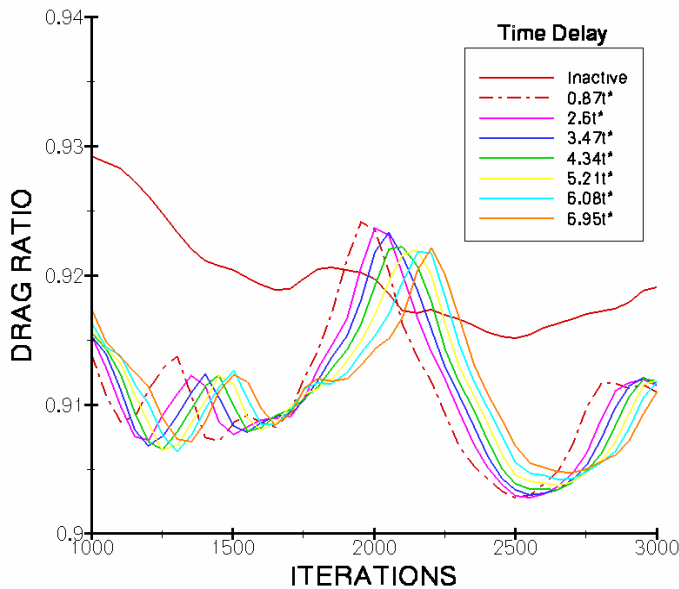


Figure 10. The results of a short simulation show the drag ratio of inactive case compared to that of the active case with various time delay constants (Δt) imposed. Results show varying the time delay has very little effect on the reduction mechanism. Longer delays result in the drag trace to be shifted more to the right, however the general characteristic of the resulting reduction mechanism is similar to that at any other delay, supporting the finding that the time delay imposed on the simulation does not effect the general result of a drag reduction.

In the previous two sections, we determined the optimal signal gain ($P_{amp} = 0.5$) and found that the time delay ($\Delta t = 182$ time steps) is not tightly constrained for the current control algorithm. Thus, a randomization test of the sensors to actuators was conducted to check whether random blowing/suction resulted in any drag reductions. That is, each sensor was connected to a random actuator instead of to the actuator in its own control unit. A successful algorithm using this randomization would contradict the current argument for an effective control algorithm. The random assignment of sensors to actuators was performed and a short simulation of approximately 15,000 iterations was conducted. The results confirm the effectiveness of the current control technique as the randomization process resulted in no large affect on the drag. Figure 11 shows the drag trace of this short test whereby control in the active and random cases where both turned on at the first iteration and both have the same gain, $P_{amp} = 0.5$. These cases are compared to the inactive case. One can see, from Fig. 11, that the random case closely follows the inactive case, at best. Comparison to the active case shows the difference between our current algorithm and that of random blowing/suction and suggests that a well-defined control algorithm has the potential to produce a drag reduction.

Using these results the next step was to run a longer simulation to 960,000 iterations (or $2605t^*$) to view the long-term effects of the control algorithm for the mean near-wall channel flow.

4. Mean and RMS Profiles

Next we examine the mean and root-mean-squared velocity profiles by averaging our results over time and across the spanwise and streamwise directions. The resulting profiles are compared with those of Kim et al.²³ and with those on the opposing flat wall of the channel. Figure 12 contains profiles showing three cases of interest which include; inactive control, active control, and the flow over the opposing smooth flat wall. By inactive control we mean that the driving membranes are present but do not move. These mean velocity profiles show negligible differences from one another.

The active and inactive profiles do not show data points below $y^+ \approx 2.1$ due to the resolution difference of the grid near the controlled surface and opposing flat wall. Since the controlled surface is created using the immersed boundary method of Goldstein et al.¹⁹ at approximately $14.8l^*$ above the computational domain boundary (see Fig. 4-5) the grid cells are larger than at the opposing flat wall. The flat portion of the profile very close to the wall is a result of grid resolution.

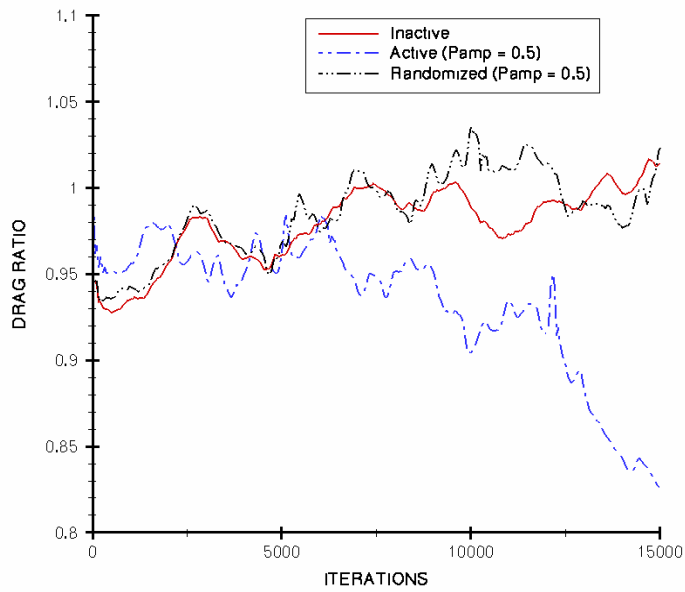


Figure 11. Drag traces comparing the inactive, active, and random cases all beginning at the same restart point at iteration 0. Control for the active and random cases (Pamp = 0.5) are both begun at iteration 0. As expected, the random control results in a trace very similar to the inactive case and supports the case for a well-defined control algorithm to reduce the drag on a controlled surface.

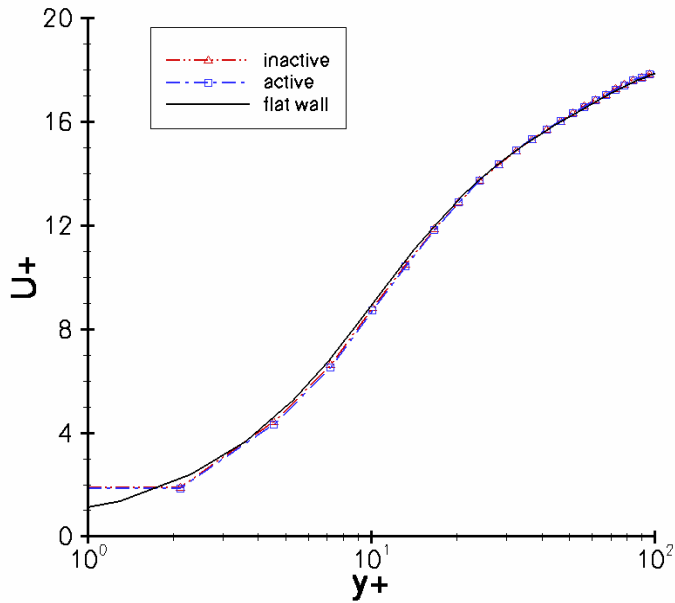


Figure 12. Mean velocity profile of streamwise velocity normalized by u^* . The profiles for the inactive, active, and opposing channel flat wall are shown using a semi-log plot.

In Fig. 13, root-mean-square velocity fluctuations are normalized by u^* . In comparing the characteristics of the flat wall profile to those of Kim et al.²³ excellent agreement is found for the u_{rms} data. A slight difference in the v_{rms} and w_{rms} data is observed in that the peak magnitude of these profiles is ≈ 0.2 less than those of Ref. 23. However, this is most likely due to our choice of consistent friction velocity and viscous length scales for normalizing all the data, and to the fact that our $R^* = 116$ is very low for turbulent channel flow. The main point is that the general trends follow those of a turbulent channel flow. In comparing the three cases of Fig. 13, one can see how simply having the altered control surface with inactive actuators results in a slight decrease in the streamwise velocity fluctuations near the surface ($y^+ < 34$). With active control, this profile is further reduced. No significant changes for the other two velocity fluctuation components are noticed in the near-wall region except for the small deviation from the flat wall profile for v_{rms} at $y^+ < 3$. This deviation is due to the fact that the controlled surface contains an array of actuator slots which weakly blow/suck fluid through portions of the wall (the slots). This could result in all three velocity fluctuation components having a non-zero mean value at $y^+ = 0$. Table 2 summarizes the values of the root-mean-squared components of velocity at $y^+ = 0$.

The Reynolds shear stress normalized by u^{*2} is shown in Fig. 14. In comparison with the results of Kim et al.²³, the peak Reynolds shear is slightly less (~ 0.1) which is consistent with the slightly smaller root-mean-squared (rms) velocity fluctuation profiles of Fig. 13. The location of peak Reynolds shear occurs at $y^+ \approx 28$ which is also consistent with Ref. 23. Very close to the surface there is little difference between the flat wall and inactive cases; however, one can see that the active case is somewhat larger than the others at $y^+ < 5$. This increase in Reynolds shear stress near the surface suggests an increase in eddy viscosity near the wall which is not clearly consistent with our control producing a small skin-friction drag reduction.

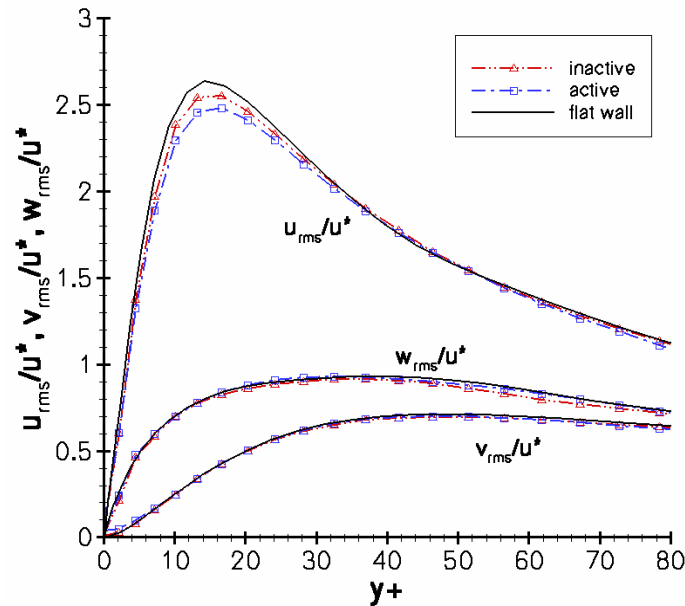


Figure 13. Root-mean-square velocity fluctuations normalized by the friction velocity, u^* , and shown in wall coordinates. Near-wall profiles of opposing channel flat wall are compared to the inactive and active control case.

Table 2. Summary of velocity data at the control surface ($y^+ = 0$).

Quantity	Inactive case	Active case	Flat wall
u_{rms}^+	0.066	0.102	0
v_{rms}^+	0.008	0.364	0
w_{rms}^+	0.022	0.026	0
$\langle -uv \rangle / u^{*2}$	0.0005	0.017	0
$\omega_{xrms} t^*$	0.042	0.068	0.16
$\omega_{yrms} t^*$	0.012	0.018	0
$\omega_{zrms} t^*$	0.116	0.123	0.345

Figure 15 shows the root-mean-square vorticity fluctuations normalized by t^* . The flat wall profiles are in excellent agreement with those of Ref. 23. The characteristic trends are all similar with a slight difference between the slotted and flat surface in peak values for the x- and z-components. The inactive and active cases differ only slightly from the flat wall profile below $y^+ \approx 8$ perhaps partly due to different grid resolution. Of course, a small portion of slip-surface over each actuator is averaged into each of these quantities. The sharp decrease in the x- and z-components immediately below $y^+ \approx 2$ is explained by the large grid cells of these cases so close to the surface. Between $y^+ \approx 2$ and $y^+ \approx 8$ the x-component is increased for the inactive and active cases with the active case being slightly larger than the inactive. In the case in inactive actuators, this slightly elevated ω_{xrms} may be due to the actuators in the surface increasing the streamwise vorticity fluctuations simply by causing the slight dipping-down of fluid over an actuator slot. For the active case, this increase is perhaps explained by the same cause or by the operation of the actuators which produce vorticity along the actuator slot lips when activated on a detected structure.

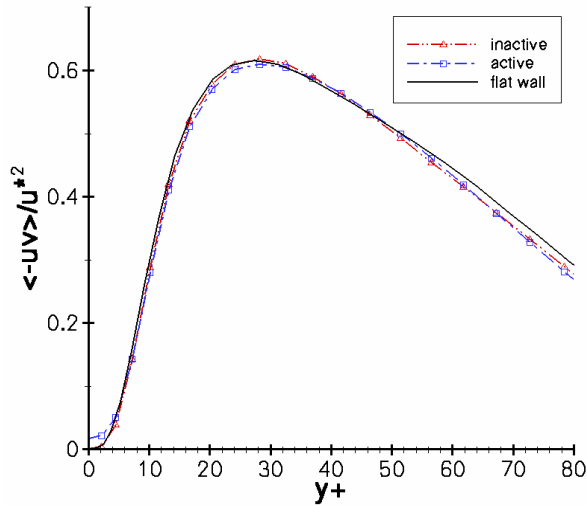


Figure 14. Reynolds shear stress for flat wall, inactive control, and active control normalized by the friction velocity, u^* and shown in wall coordinates.

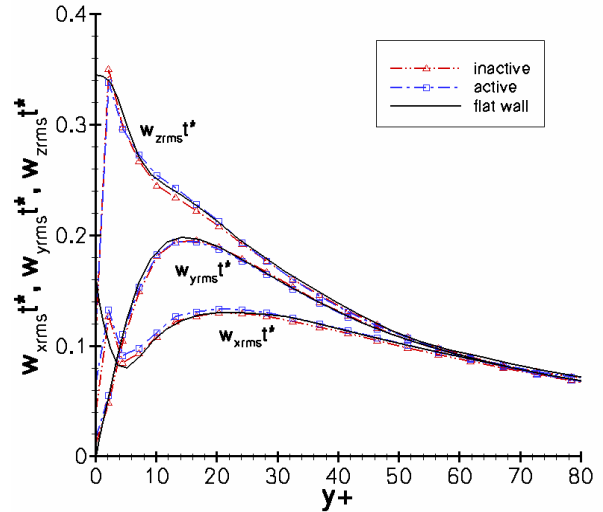


Figure 15. Root-mean-square vorticity fluctuations normalized by t^* and shown in wall coordinates. Profiles of a smooth flat wall are compared to the inactive and active control case.

Having examined the time-averaged profiles one finds there is little to distinguish between the three cases. The profile characteristics agree fairly well to those established in Ref. 23 for turbulent channel flow. The main observation however is that, for our low Reynolds number, the profiles contain the characteristics of a turbulent channel flow.

In the next section we try to gain an understanding of the physical mechanisms at play in the near-wall region. The review of the time averaged, spanwise and streamwise averaged data show that the near-wall region is weakly affected by our current array of actuators for both the inactive and active cases. Table 2 summarizes the data at the

control surface to show how certain quantities compare for the three cases. Next we look at cross-sectional views of the computational domain to try to put physical meaning into the characteristics show above.

5. Cross Sectional Data

It is beneficial to examine the physics of what is occurring in the near-wall region. We attempt to show the phenomena by using six sets of cross sectional views of the 3-D domain at various instances in time. Figure 16 consists of a wall-parallel plane located at $y^+ \approx 2.125$, which coincides with the height of our detection region. On this plane, contours of wall-normal velocity are shown to pin-point the timing and strength of the actuation events. Crossing this plane are three cross sections of data located at the streamwise location of detection ($x^+ = 609$), across the center of the row of actuators ($x^+ = 729$), and finally at a symmetrical distance downstream of the actuator row ($x^+ = 849$). These three planes show enstrophy ($(\omega)^2$) to easily view regions of low and high shear stress near the surface. Black vectors indicate the wall-normal velocity at the slot exit plane; their size is exaggerated compared to the white vectors in the three y-z planes. A final important note is that only the middle row of actuators is shown in the figure. The choice of which row to zoom-in on is arbitrary but such a close-up is necessary to view the details of the flow over the array of actuators.

The illustrations of Fig. 16 cover a small instance in time toward the beginning of a simulation run using $\Delta t = 425$. This amount of delay accounts for the convection of the detected structure to the center of an actuator. The first frame with $t_{\text{ref}} = 0$ corresponds to $t = 11.5t^*$ after control was first turned on. In this frame a sweeping structure identified as “A” is shown at the detection region and is shown to approach slot # 4. Observation of the near-wall enstrophy just below structure “A” reveals a large high-shear stress region on the surface. The actuation event associated with the detection of structure “A” is shown in the following frame with $t_{\text{ref}} = 11.5t^*$. The expected response of actuator #4 is a blowing action since it seems logical to blow at sweep events to deflect high-speed fluid away from the surface. At $t_{\text{ref}} = 11.5t^*$ one sees the strong sweep event dominates over the slot action resulting in a net down flow over most of the actuator. However, a blowing action was performed by the actuator as can be seen with small red contour region to the left side of actuator #4. This is a key observation for the current control algorithm because the magnitude of the actuator gain, P_{amp} , was set such that we do not have strong individual jet-pulses of fluid exiting or entering the actuator. Instead the current method aims to create small disturbances or ripple-like effects on the control surface to make the near-wall flow less unstable -the goal is not the immediate local reduction of high-shear stress regions to reduce the skin-friction drag. The effects of the actuation are seen in frame $t_{\text{ref}} = 23.1t^*$ where a high-shear region still exists downstream of slot 4; however, one should note how the spanwise width of the high-shear region has decreased from $x^+ = 609$ to $x^+ = 849$. At $x^+ = 849$ it appears the high-shear region is shorter in the spanwise direction but higher in the wall-normal direction.

Referring back to $t_{\text{ref}} = 0$, structure “B” is illustrated as a general low-speed region as with velocity vectors slightly pointed up but mainly directed in the positive z-direction. One can see the corresponding low enstrophy region below “B” on the wall. At $t_{\text{ref}} = 11.5t^*$ the proper control, suction, is applied to counter the weak counter-clockwise vortex above slots #4 and 5 and allows the low-shear region at the wall to continue downstream which is observed at $x^+ = 849$ at $t_{\text{ref}} = 23.1t^*$. Structure “C”, pointed out at $t_{\text{ref}} = 0$, is another example of a high enstrophy or high-shear stress region at the wall with an associated sweep event of high-speed fluid. This structure seems to approach slot #1 and appears to have reached the actuator at $t_{\text{ref}} = 11.5t^*$. As expected the actuator response is a blowing action which seems to effectively counter the sweep event keeping the high-shear region away from the control surface. The high-shear region persists as seen at $t_{\text{ref}} = 23.1t^*$ at the downstream cross plane. While the velocity vectors appear deflected away from the wall, high-shear stress is still observed just below the structure.

Another set of interesting structures are shown at $t_{\text{ref}} = 23.1t^*$. Structure “E” seems to be counter-clockwise vortex which has a sweep region approaching slot #3 and causing a high-shear region at the wall. The appropriate blowing response is shown at $t_{\text{ref}} = 34.6t^*$; with the addition of a suction response of actuator #2 both seem to counter the wall-normal velocity vectors just above the surface. The actuator response does not noticeably effect the high-shear region which persists at $t_{\text{ref}} = 46.1t^*$. Structure “D” is a net downwash region associated with a pair of counter-rotating vortices. A high-shear region is shown to approach between slot #4 and 5 with a clockwise vortex toward the left of the sweep event and centered at approximately $y^+ = 20$. A weaker counter-clockwise begins to form to the right. At $t_{\text{ref}} = 34.6t^*$ a pair of counter-rotating vortices is clearly observed over slot #4. The suction of actuator #4 and blowing of #5 have an effective influence on the weak pair. Observing the structure at the downstream plane at $t_{\text{ref}} = 46.1t^*$ one observes one large counter-clockwise vortex centered over the spanwise location of slot #4.

Both of the structures “G” and “F” illustrated in $t_{\text{ref}} = 34.6t^*$ show high-shear regions at the wall. Structure “G” is clearly a pair of counter-rotating vortices while “F” seems to show a very weak pair of vortices. The actuator response is consistent with those already observed. Structure “F” approaches between slots #4 and 5 and the actuator

pair again shows opposite actuation with fluid exiting at slot #5 and suction at slot #4 at $t_{ref} = 46.1t^*$ which appears to create an opposite vortex to the weak counter-clockwise vortex above slot #5. Observing this high-shear region “F” at $t_{ref} = 57.7t^*$ supports the previous observation of the structure shifted toward the actuator with suction applied. The final structure illustrated here is “G” which is a pair of counter-rotating vortices approaching slots #2-4. Suction of actuator #2 and #4 and blowing of #3 is consistent with the velocity opposition approach as each seem to counter the wall-normal velocities at $y^+ = 10$. This opposition is shown at $t_{ref} = 46.1t^*$ with varying degrees of actuation across the three actuators. The clockwise vortex dissipates by the time the structure reaches $x^+ = 849$ at $t_{ref} = 57.7t^*$ and a single counter-clockwise vortex remains.

While the series of illustrations of Fig. 16 do not show a general trend towards the reduction of eddies downstream of the actuator row, specifically in the near-wall region, the picture becomes more clear if we look at the time-averaged data over the entire simulation duration at a wall-normal height of approximately $y^+ = 2$ as illustrated in Fig. 17. In Fig. 17 we time average the entire $2606t^*$ of data and plot the streamwise velocity component, normalized by the friction velocity.

One immediately sees the streamwise acceleration of fluid over each actuator. This is consistent with the notion of altering the no-slip boundary with small portions of a slip-like boundary condition over each recessed cavity. Moreover, even with the active case, the boundary condition over the individual actuators is slip-like and regions of higher streamwise velocity result. In comparing the two cases, Fig. 17a shows very persistent, long streamwise structures covering the entire length of the domain and spaced approximately $50l^*$ in the spanwise direction. This seems to indicate the presence of the long low-speed streaks characteristic of turbulent wall flow but that we have not run our simulation long enough to obtain the more uniform streamwise velocity contours expected in a time-averaged data set. Figure 17b shows the active case and one observes how the long streamwise streaky structures are broken up into shorter, thinner structures which extend at most a third of the domain length. This may indicate that small amplitude actuation is enough to break up the long coherent near-wall structures typical of turbulence.

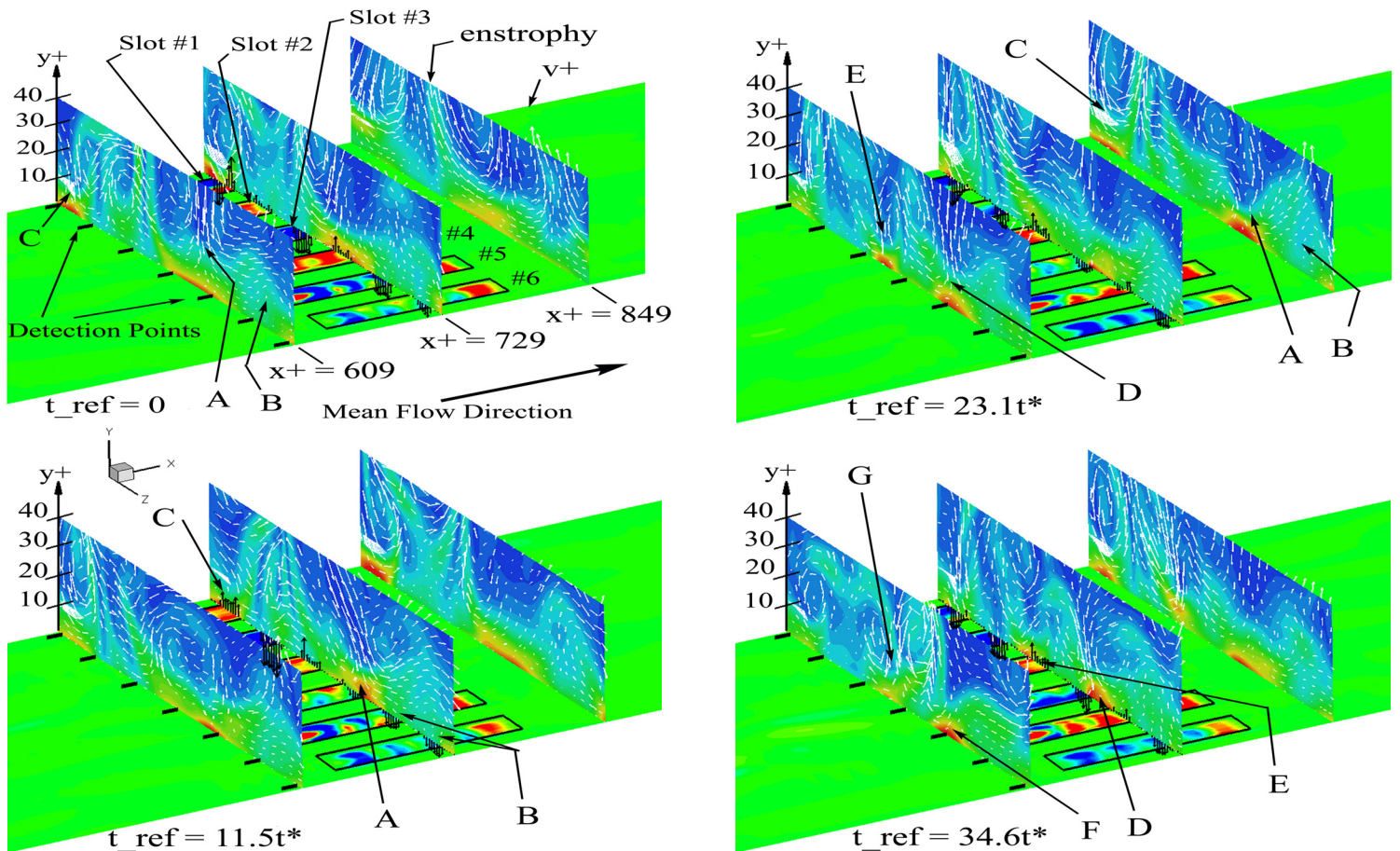


Figure 16. Caption on following page.

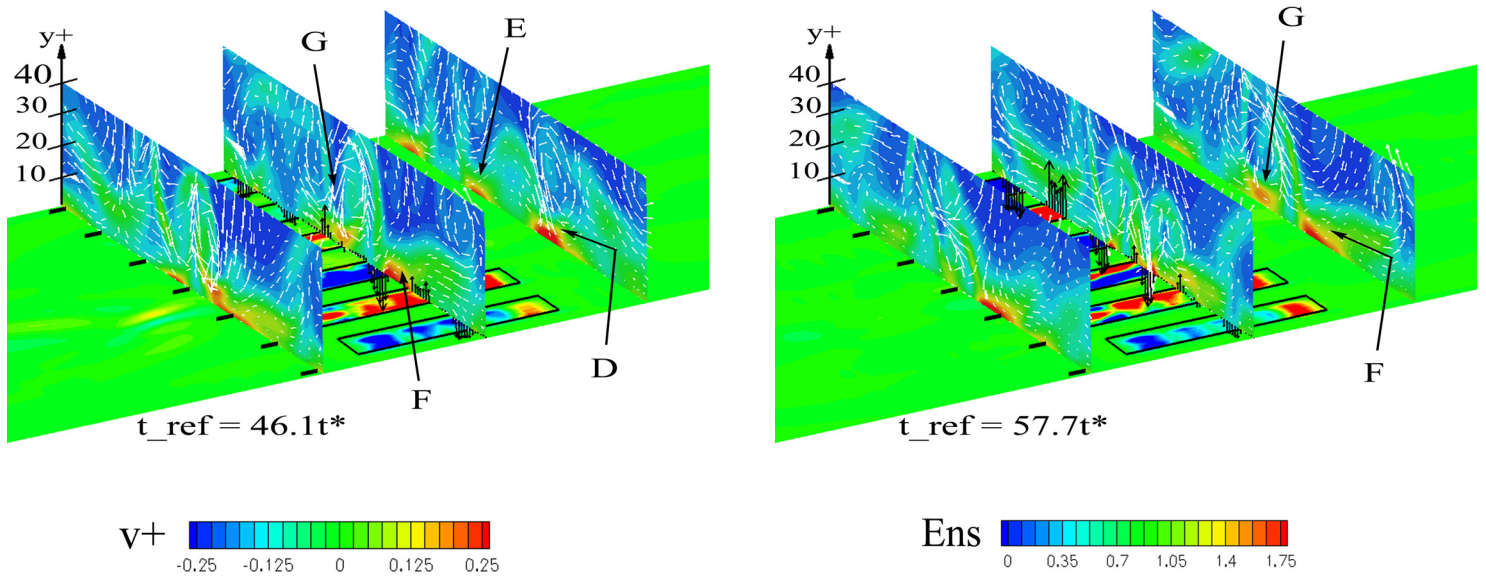


Figure 16, continued. Cross-sectional compilation of data to illustrate near-wall vortical structures. Detection events at $x^+ = 609$ are shown with the corresponding actuation event at $x^+ = 729$. Downstream effects of actuation are shown at $x^+ = 849$. Slices along the x - z plane display contours of wall-normal velocity while y - z slices show contours of enstrophy. This series of illustrations begins $11.5t^*$ after the control was first turned on. Vectors show velocities in plane. Black vectors showing slot suction or blowing are exaggerated compared to the white vectors.

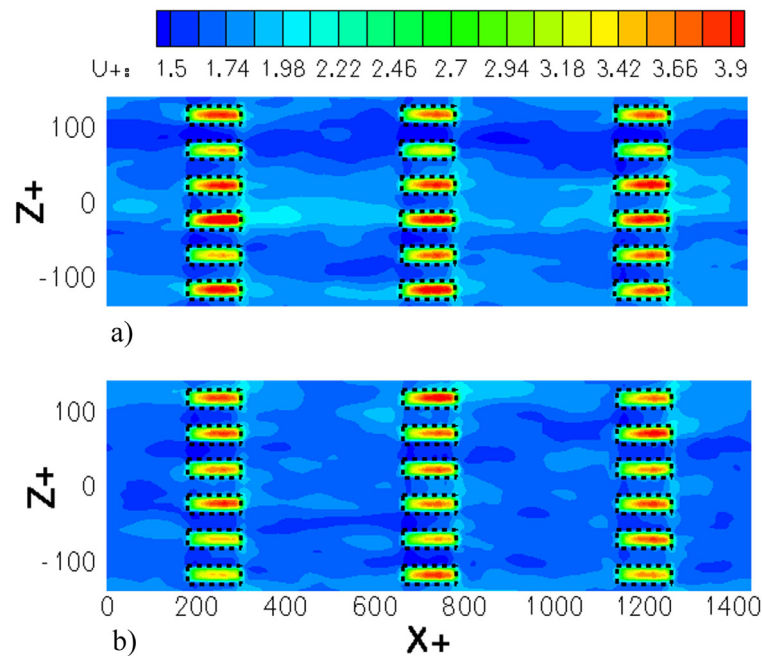


Figure 17. Time-averaged contours of streamwise velocity on an xz -plane located at $y^+ \approx 2.1$ above the controlled surface for: (a) inactive case ($Pamp = 0.0$) and (b) active case ($Pamp = 0.5$).

Figure 18 shows the time and spanwise averaged contours of streamwise velocity on the x - z plane located at $y^+ \approx 2$. By averaging in the spanwise direction the long streaks are no longer present and a better view of the flow near the actuators is gained. As observed in Fig. 17, streamwise acceleration of the flow is shown over the actuators. Also notice that beside each actuator is a region of lower speed fluid which occurs as the acceleration of fluid over an actuator slightly entrains the surrounding flow resulting in an inward turning of the velocity streamlines towards the

center of the actuator. The spreading streamlines result in a smaller streamwise component of velocity for the regions adjacent to the actuators.

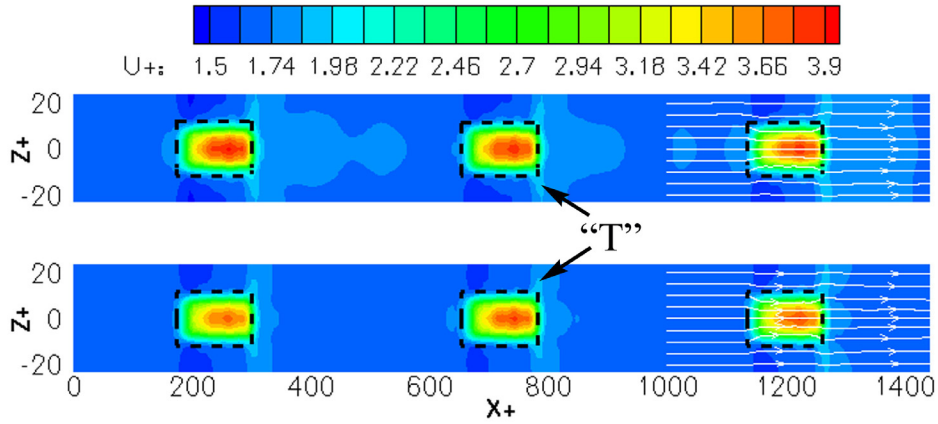


Figure 18. Time and span-averaged contours of streamwise velocity on an xz -plane located at $y^+ \approx 2.1$ above the controlled surface for: (a) inactive case and (b) active case. Note the stretched z^+ length scale.

Also noticeable is that these low-speed regions seem to be dominant towards the upstream half of the actuators. This may be explained by the characteristic dipping of the streamlines into a cavity. The streamlines dip down just aft of the cavity leading edge and entrain the surrounding fluid which causes the deceleration of fluid between actuators. At the downstream end of the cavity the streamlines rise up and out. There, the upward shift in the streamlines compresses the streamlines beside the slot thus producing faster moving fluid surrounding the downstream end of the actuator. This is seen as the characteristic “T” shape of the surface shear stress patterns at the trailing edges of the actuators. A final observation of Fig. 18 is, in the case of active control, the general shortening of the high speed fluid regions directly downstream of the actuators. This is consistent with regions of reduced shear stress and the overall reduction of skin-friction drag.

6. Drag Reduction

To quantify the performance of the control algorithms a simple ratio is used to compare the shear stresses on the top, un-actuated channel surface and the bottom surface which includes our flow control mechanism. This drag ratio is

$$\text{Drag Ratio} = \frac{D_{\text{actuated side}}}{D_{\text{top wall}}} \quad (4)$$

A drag ratio of less than 1 means the control algorithm is working to reduce the skin-friction drag of the manipulated bottom surface. Figure 19 shows the drag ratio trace and running average for the current control algorithm. The figure compares an inactive versus an active case. The simulation was run to 96,000 iterations, which is equivalent to $2605t^*$.

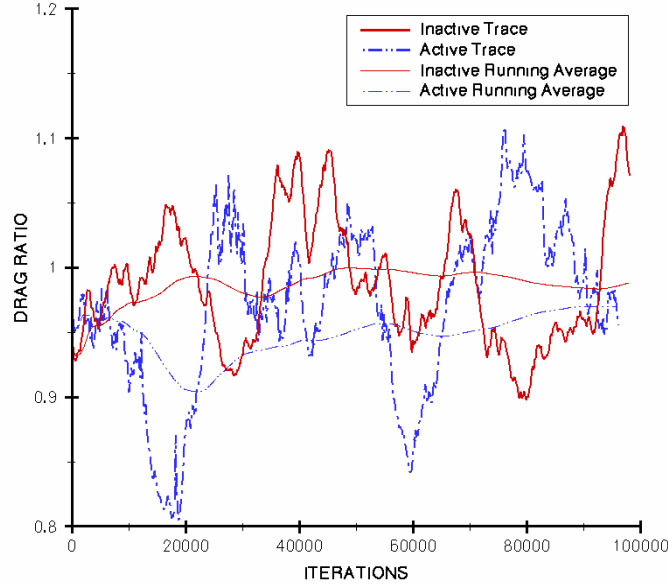


Figure 19. Drag reductions for the inactive and active cases. Shown is the drag trace and running average for each for time duration of approximately $2606t^*$.

The running averages of both cases suggest a small drag reduction throughout the duration of the simulation. As seen in the figure the drag trace for the inactive case jumps by $\pm 10\%$ while that of the active case peaks at $+10\%$ (increase) and dips as low as -20% (reduction). In general, there seems to be an intermittency period of roughly every 15,000 iterations. Fifteen thousand iterations is equivalent to the flow convecting almost three times the length of the domain using the average convection speed of structures at $y^+ \sim 10$. The general trend shown in the running average is that while the initial control resulted in a large reduction ($\sim 10\%$), over longer periods of time the control will settle to a very small drag reduction value of just a couple of percent.

For the duration of the simulation above, active control provides a small drag reduction of $3\% \pm 2.1\%$ whereas the average reduction of the inactive case is $1.2\% \pm 1.4\%$. These results are in good agreement with those of Lee²⁶ which uses the same immersed boundary layer technique and actuators but a different control methodology of detecting vertical fluctuations over the slots and applying opposition control. These data are summarized in Table 3. A final note is that the figure shows that the running average is still not completely stable at 96,000 iterations which suggests that the simulation has not been run long enough and a simulation out to $\sim 300,000$ iterations may be needed to achieve a good statistical average.

Table 3. Average drag reductions for different cases compared to Lee.²⁶ The number of independent realizations is determined through an auto correlation of the drag.

<i>Case</i>	<i>Indep. Realizations</i>	<i>Average Drag Reduction</i>	<i>Standard error</i>
Inactive ($Pamp = 0.0$)	12	1.2%	$\pm 1.4\%$
Active ($Pamp = 0.5$)	10	3.0%	$\pm 2.1\%$
Inactive, Lee result ²⁶	10	1.1%	$\pm 3.8\%$
Active, Lee result ²⁶	38	4.6%	$\pm 1.3\%$

We now move on to the investigation of a second control algorithm which also utilizes flow information at the wall. The algorithm is easier to comprehend physically as we will target the streamwise component of the high- and low-shear stress regions upstream of the actuators which correspond to sweep and ejection events. Comparison of the two control algorithms may help to confirm that multiple detection quantities can be associated with the coherent near-wall structures and that the use of one over the other may result in larger drag reduction.

B. Detection of $(\partial u / \partial y)|_{\text{wall, average}}$
1. Overview of Control Algorithm

Here we present preliminary results using a second detection method based on the experiments of Lew et al.¹⁷ The main objective of this scheme is to detect high- and low-shear stress regions just upstream of a micro-actuator and manipulate the near-wall flow such that the near-wall coherent structures are weakened. In contrast to the previous detection method, the sensors are modeled as hot-wires aligned in the spanwise direction. The streamwise component of velocity is averaged over 16 detection points covering a spanwise width of $23l^*$, equivalent to the width of a single actuator, at approximately $2.125l^*$ above the surface. The high- and low- shear regions are determined by comparing this averaged velocity ($u_{\text{avg, measured}}$) to $u_{\text{top wall}}^+$ evaluated at $2l^*$ over that surface. Using the law of the wall approximation $u_{\text{top wall}}^+$ is equal to $u^+ \approx y^+ \approx 2.125$. Equation 5 summarizes the calculation involved in determining whether a high- or low-shear region is approaching an actuator.

$$\frac{\frac{u_{\text{avg, measured}}}{u^*}}{\frac{u^+}{u^*}} - 1 \Rightarrow \frac{\frac{u_{\text{avg, measured}}}{u^*}}{u^+|_{y^+=2.125}} - 1 = \begin{cases} > 0 & \text{high - shear region} \\ = 0 & \\ < 0 & \text{low - shear region} \end{cases} \quad (5)$$

$$(v_{\text{blowing/suction}})_{\text{time=t}} = (P_{\text{amp}}) \cdot (C_{\text{deflection}}) \cdot \left[\frac{\frac{u_{\text{avg, measured}}}{u^*}}{2.125} - 1 \right]_{\text{at time=t}-\Delta t} \quad (6)$$

Equation 6 shows that a positive value in Eq. 5 will result in a blowing of the actuator in order to deflect away some of the high-speed fluid sweeping towards the wall. Conversely, a negative value in Eq. 5 will direct the actuator to provide suction to a low speed streak thereby reducing the ejection of this fluid away from the wall, hopefully weakening the streak and perhaps keeping it stable.

Shown in Fig. 20, the placement of the sensors is approximately $38l^*$ upstream of the actuator leading edge. The actuating mechanism and spacing between actuators remains the same as the previous scheme. While a parametric study of the actuator gain signal, P_{amp} , and the time delay variable, Δt , has yet to be completed, the next section provides preliminary results using a $P_{\text{amp}} = 0.01$ which seems to have resulted in an insufficient actuation strength; however, setting P_{amp} to five times this value resulted in what looked to be increased fine scale turbulent structures near the wall. A $\Delta t = 375$ is also set which is equivalent to the time it takes a structure to convect from the sensing region to the center of the actuator.

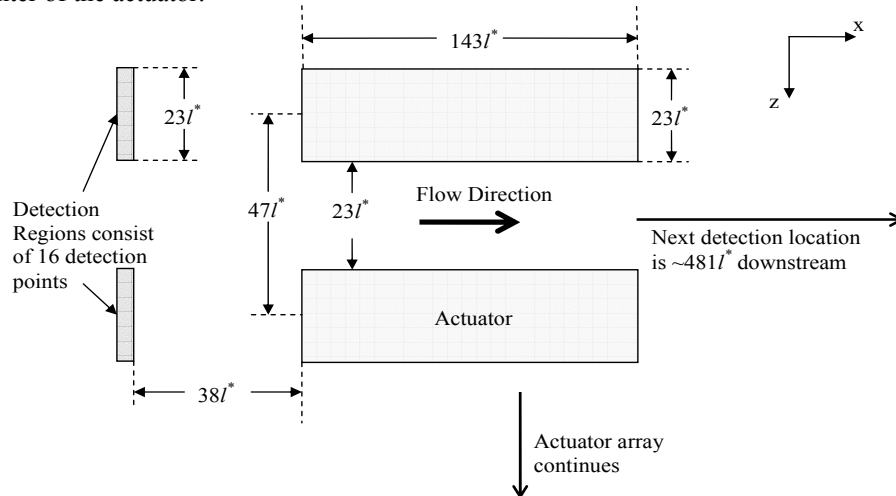


Figure 20. Summary of spatial dimensions of detection scheme. Shown is only a partial section of the controlled surface. The average over 16 detection points (modeled as a grey hot-wire aligned in the spanwise direction) is used to sense high- and low- shear regions just upstream of an actuator. A time delay variable is introduced into the control algorithm so that the time it takes a structure to convect from the sensor to the center of the actuator ($110l^*$) is accounted for. Actuator dimensions follow those suggested in Ref. 14 and 18.

2. Cross Sectional Data

In Fig. 21 we look at a series of illustrations and examine a few specific structures and the effect control has on them. In contrast to Fig. 16, here we plot contours of the streamwise velocity component in the plane at $y^+ = 2.125$. Also shown at $x^+ = 609$ are the individual detection regions marked in white at the wall. Because the current detection scheme looks for low- and high-shear regions, plotting the streamwise velocity component allows a clear illustration these events. The series of illustrations begins $380t^*$ after the control was first turned on, therefore the following results are preliminary and we do not bother to examine time-averaged and span-averaged data for this reason. Beginning with $t_{\text{ref}} = 0$, we first note the high-speed streaks detected approaching slots #4-5. The high-speed streamwise velocity contours match very well with the contours of enstrophy in the cross-sectional view which shows two distinct regions of high enstrophy at $x^+ = 609$. Structure ‘‘A’’ is a high-shear event which approaches slot #5; note that directly above this event is what seems to be a sweep event of higher speed fluid from the center of the channel. This helps to confirm that a downward sweep of fluid near the surface corresponds to a high enstrophy region or high-shear stress.

The next frame at $t_{\text{ref}} = 5.1t^*$ is an intermediate frame to show an ejection event labeled as structure ‘‘B’’ just above the detection region of slot #3. The event is associated with a low enstrophy and therefore low-shear stress region at the wall which follows the convention that ejection events leave behind regions of low-speed fluid on the wall. At $t_{\text{ref}} = 10.2t^*$ structure ‘‘A’’ has reached the center of the actuator and the resulting actuation of slot #5 is blowing, shown by the wall-normal velocity vectors in black. This helps to confirm that Eqs. 5 and 6 employ the correct sign and in general work as they are expected. For now we skip to $t_{\text{ref}} = 20.3t^*$ which shows structure ‘‘A’’ downstream of actuator #5; note that a sweep event still exists and that this event has not shifted in the spanwise direction. However, also note how the high-shear region and another associated with slot #4 have remained roughly the same as they were upstream of the actuators at $t_{\text{ref}} = 0t^*$. Now, at $t_{\text{ref}} = 20.3t^*$, they have become larger. This suggests that while we have a reasonable control methodology, the scheme has not worked to decrease the near-wall shear stress.

Looking at $t_{\text{ref}} = 15.2t^*$, structure ‘‘B’’ has reached actuator #3 and for a detected ejection event at $t_{\text{ref}} = 5.1t^*$ we perform the correct control, suction, on the ejection event over slot #3. The ejection of fluid is still present however at $t_{\text{ref}} = 25.4t^*$ with high enstrophy regions on the wall and to both sides of the ejection event. A final structure examined is structure ‘‘C’’ of $t_{\text{ref}} = 15.2t^*$, where a counter-clockwise vortex is observed approaching slots #5-6. A high enstrophy region on the control surface is observed on left, sweeping side of the vortex while the right, ejecting side shows low enstrophy, as expected. The center of the streamwise vortex is located at approximately $y^+ = 20$. Structure ‘‘C’’ reaches the actuator center at $t_{\text{ref}} = 25.4t^*$ where the streamwise vortex is still present between slots #5-6 and its center seems to be closer to the wall at approximately $y^+ = 10-15$. Based on the detection of the event at $t_{\text{ref}} = 15.2t^*$ the control interprets a low-shear stress region approaching slot #6 and a mixed low-and high-shear stress region approaching slot #5. This results in suction at both slot #5 and 6 which is not what is needed to counteract the vortex now present at $t_{\text{ref}} = 25.4t^*$. Of course the gains of our actuation are small and it seems that they are too small in the case shown here; however, in general our methodology is to create small ripple-like disturbances close to the wall which are best described as small bulges and dips over the actuators. Consequently, our applied actuation at slots #5-6 is not enough to disrupt the streamwise vortex as it is still present at $t_{\text{ref}} = 35.5t^*$.

In comparing the two control algorithms examined herein (detecting $\partial\tau_z/\partial z$ vs. τ_x) it seems that neither method immediately reduces the high enstrophy regions at the control surface. However, in contrast to the $\partial\tau_z/\partial z$ method, the τ_x method appears to slightly increase these regions. This is best seen by observing how the bright red regions at $x^+ = 609$ evolve as they reach $x^+ = 849$ in Figs. 16 and 21. Therefore, preliminary results show that a drag reduction is not achieved in the current simulation which was run for 26,000 iterations or $706t^*$. Instead, a drag *increase* of $1.6\% \pm 0.9\%$ is observed. The data are summarized in Table 4 along with a test case run for 24,000 iterations using a smaller $Pamp = 0.005$. Comparison with the previous control results and the data of Lee²⁶ can be made by referring to Table 3.

Table 4. Average drag reductions for preliminary test run.

Case	Indep. Realizations	Average Drag Reduction*	Standard error
Active ($Pamp = 0.005$)	4	-0.7%	$\pm 2.2\%$
Active ($Pamp = 0.01$)	8	-1.6%	$\pm 0.9\%$

*a negative number indicates a drag increase.

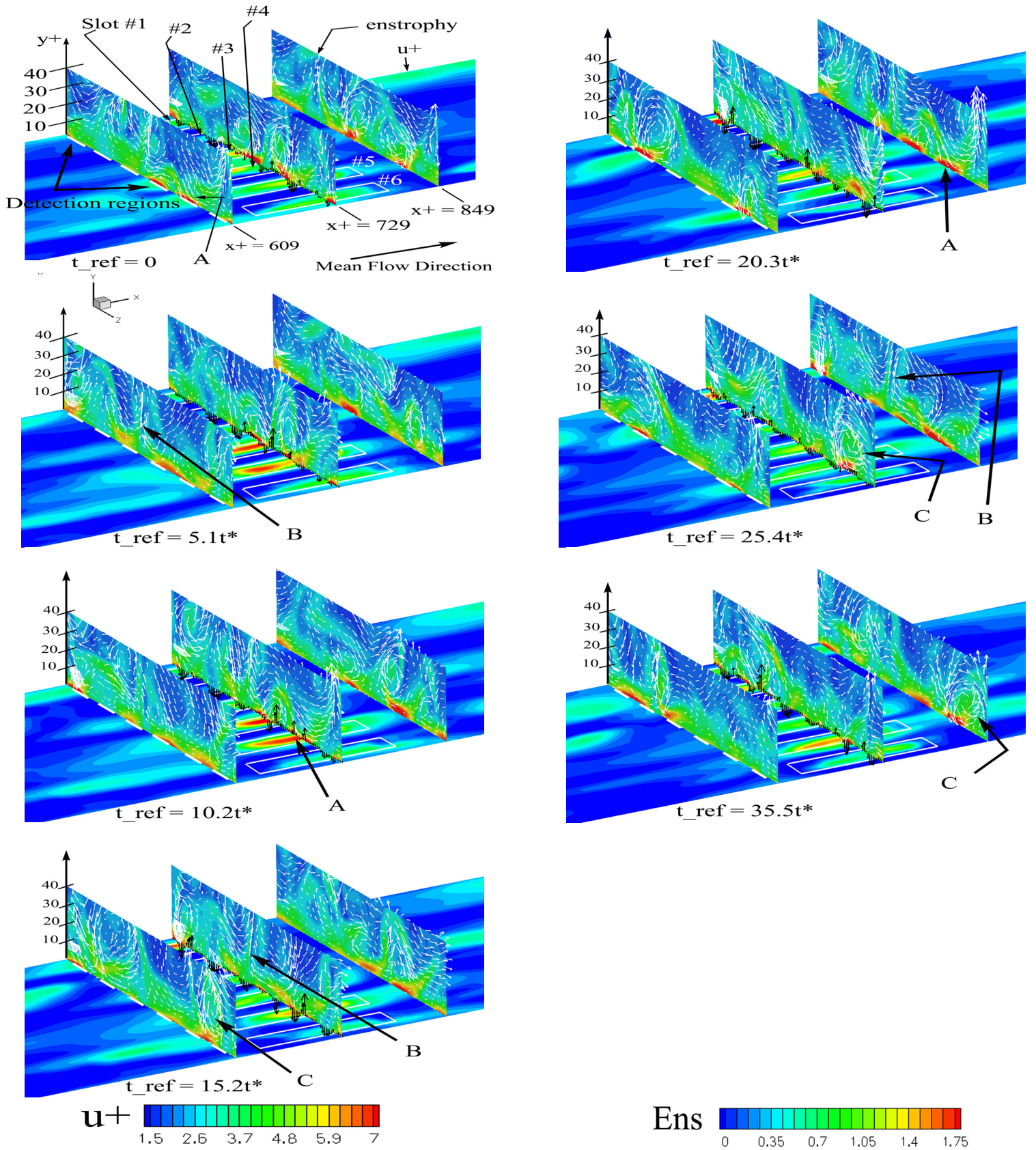


Figure 21. Cross-sectional compilation of data to illustrate near-wall vortical structures. Detection events at $x^+ = 609$ are shown with the corresponding actuation event at $x^+ = 729$. Downstream effects of actuation are shown at $x^+ = 849$. Slices along the $x-z$ plane displays contours of streamwise velocity, normalized by u^* , while $y-z$ slices show contours of enstrophy. This series of illustrations begins $380t^*$ after the control was first turned on. Vectors show velocities in plane. Black vectors showing slot suction or blowing are exaggerated compared to the white vectors.

IV. Conclusion

The objective of this paper was to design a physically practical control algorithm based on previous numerical and experimental work in the field. We aimed to design a control which would produce small disturbances very close to the control surface with the goal of quieting the near-wall vortical structures responsible for the regeneration and maintenance of turbulence. As a result, two control algorithms were examined, both based on detection of a quantity at the wall. The first method used detection of $\partial/\partial z(\partial w/\partial y)|_{\text{wall}}$. In addition, preliminary results of a second control scheme using the detection of $(\partial u/\partial y)|_{\text{wall}}$ were examined. Results after 96,000 iterations for the detection of $\partial/\partial z(\partial w/\partial y)|_{\text{wall}}$ produced a small $3\% \pm 2.1\%$ reduction in drag with actuation turned on while a small $1.2\% \pm 1.4\%$ reduction was observed for the inactive actuators. Both results are comparable to the reductions of similar test cases produced by Lee²⁶. In those cases, the same immersed boundary technique of Goldstein et al.¹⁹ was used but his control algorithm was based on that of Choi et al.⁸ The main objective of Lee²⁶ was to dampen the velocity fluctuations just above an actuator by sampling v -velocity at a detection area above each actuator, but well within the flow, and apply a continuous blowing/suction to achieve v -velocity fluctuation dampening in these regions. Both control designs, that of Lee²⁶ and the method of $\partial/\partial z(\partial w/\partial y)|_{\text{wall}}$, cover approximately 15% of the total channel surface by using an array of 18 actuators evenly spaced in three rows on the control surface. The small percentage of control surface covered by actuators explains why the drag reductions achieved in both control designs are small compared to the $\sim 25\%$ drag reductions reported by Choi et al.⁸ The method of Choi et al.⁸ dampened the v -velocity fluctuations at *every* grid point on a detection plane and continuous blowing/suction was applied over the *entire* channel surface. Therefore, if we were to expand our array of actuators such that we covered close to the total control surface, the drag reductions reported here may be approximately 6.5 times larger, a reduction comparable to that of Choi et al.⁸

A series of parametric studies was performed to obtain an optimal actuation gain and to find the optimal time delay between the detection and actuation events. It was found that an actuation gain which resulted in $v_{\text{rms}} \approx 0.28u^*$ in the slot plane provided the greatest drag reduction over a series of short-term tests. This value falls within the root-mean-squared control jet amplitude range of $0.15\text{-}0.55u^*$ found in tests by Breuer et al.¹ and Lee et al.¹³ Surprisingly, the optimal time delay, or lag, between detection and actuation events was found to be not very important for the current control method. This may be due to the typical lengths of the velocity streaks compared to the small range of delays examined in the parametric study. Therefore, a delay corresponding to the time it takes a large scale turbulent structure to convect in the streamwise direction, at an average speed of $10.7u^*$ ¹⁴, from the detection location to the leading portion of the actuator was satisfactory.

Furthermore, in an effort to confirm the effectiveness of the control algorithm, a randomization test case was run and compared for the inactive and active cases of our $\partial/\partial z(\partial w/\partial y)|_{\text{wall}}$ control. A short-term test was performed in which each pair of sensors were randomly assigned to one of the actuators located somewhere in the array. Results show that, at best, the randomization case matched the slight reductions produced by the inactive test case. The larger drag reductions observed for the active case are not expected in the random case because randomization does not target specific coherent structures. This is reasonably consistent with the results of Dahlburg et al.²⁷ who found no drag reduction from introducing randomized body forces in a turbulent channel flow. Therefore, in examining the random case we found first, that $\partial/\partial z(\partial w/\partial y)|_{\text{wall}}$ control is an effective algorithm and, secondly, that the drag reduction confirms the idea of targeting specific turbulent structures to weaken the near-wall vortical structures responsible for turbulence regeneration.

In addition, preliminary data were reported using the second control method which detected a span-averaged $(\partial u/\partial y)|_{\text{wall}}$ quantity at the wall. While the optimal actuation gain and time delay has not yet been investigated in detail, actuation resulting in $v_{\text{rms}} \approx 0.05u^*$ (for $Pamp = 0.01$) and $v_{\text{rms}} \approx 0.025u^*$ (for $Pamp = 0.005$) with a time delay to match the convection of the detected structure to the center of the actuator were used to gather the preliminary data. The potential for drag reduction using this method does not match that of the first control method examined. With a $1.6\% \pm 0.9\%$ and $0.7\% \pm 2.2\%$ drag *increase* found thus far, it seems that the optimal gain as well as an optimal time delay may be more critical than in the previous method. Specifically, the time delay may be important here because of the detection of high-shear stress regions which typically are short compared to the long low-speed streaks. In addition, our gains tried so far seem too small.

In conclusion, the current research supports the idea of weakening the near-wall coherent structures of turbulent channel flow through the use of physically practical control devices and algorithms which make use of flow information on the wall. While the reductions reported seem small compared to other the numerical studies, it should be kept in mind that only 15% of the total surface was covered in our cases. Furthermore, by increasing the actuator population, which is feasible with current progress in MEMS technology, the potential for a significant drag reduction over a surface remains promising.

Acknowledgments

The authors gratefully acknowledge the funding provided by the Air Force Office of Scientific Research, under grant number F49620-02-1-0093 and the computation time provided by the Texas Advanced Computing Center, TACC, in support of this project. Helpful conversations with Dr. Conrad Lee are gratefully acknowledged.

References

- ¹Breuer, K. S., Amonlirdviman, K., and Rathnasingham, R. "Adaptive Feed-Forward Control of Turbulent Boundary Layers," AIAA paper 98-1025, 1998.
- ²Jimenez, J. and Pinelli, A., "The autonomous cycle of near-wall turbulence," *Journal of Fluid Mechanics*, 1999, **389**:335-359.
- ³White, F. M., *Viscous Fluid Flow*, 2nd ed., McGraw-Hill Series in Mechanical Engineering, 1991, Chap. 6.
- ⁴Panton, R., *Self-Sustaining Mechanisms of Wall Turbulence*, Computational Mechanics Publications, 1997, Chap. 2, 10.
- ⁵Koumoutsakos, P., Bewley, P., Hammond, E. P., and Moin, P., "Feedback Algorithms for Turbulence Control – Some Recent Developments," AIAA paper 97-2008, 1997.
- ⁶Goldstein, D. B. and Tuan, T.-C., "Secondary flow induced by riblets," *Journal of Fluid Mechanics*, 1998, **363**:115-151.
- ⁷Kang, S., and Choi, H., "Active wall motions for skin-friction drag reduction," *Physics of Fluids*, 2000, **12**, No. 12:3301-3304.
- ⁸Choi, H., Moin, P., and Kim, J., "Active Turbulence Control for Drag Reduction in Wall-Bounded Flows," *Journal of Fluid Mechanics*, 1994, **262**:75-110.
- ⁹Koumoutsakos, P., "Vorticity flux control for a turbulent channel flow," *Physics of Fluids*, 1999, **11**, No. 2:248-250.
- ¹⁰Carlson, H. A. and Lumley, J. L., "Active control in the turbulent wall layer of a minimal flow unit," *Journal of Fluid Mechanics*, 1996, **329**:341.
- ¹¹Lee, C., Kim, J., and Choi, H., "Suboptimal control of turbulent channel flow for drag reduction," *Journal of Fluid Mechanics*, 1998, **358**:245-258.
- ¹²Endo, T., Kasagi, N., and Suzuki, Y., "Feedback control of wall turbulence with wall deformation," *International Journal of Heat and Fluid Flow*, 2000, **21**:568-575.
- ¹³Lee, C., Kim, J., Babcock, D., and Goodman, R., "Application of neural networks to turbulence control for drag reduction," *Physics of Fluids*, 1997, **9**, No. 6:1740-1747.
- ¹⁴Rathnasingham, R. and Breuer, K. S., "System Identification and Active Control of a Turbulent Boundary Layer," AIAA paper 97-1793, 1997.
- ¹⁵Rathnasingham, R. and Breuer, K. S., "Closed-Loop Control of Turbulent Boundary Layers," *Unpublished*, Division of Engineering, Brown University, Providence, RI, 2002.
- ¹⁶Rebbeck, H. and Choi, K-S., "Opposition control of near-wall turbulence with a piston-type actuator," *Physics of Fluids*, 2001, **13**, No. 8:2142-2145.
- ¹⁷Lew, J., Huang, A., Ho, C-M., Jiang, F., and Tai, Y. C., "Surface Shear Stress Reduction with MEMS Sensors/Actuator in Turbulent Boundary Layers," *Unpublished*, Univ. of California, Los Angeles and Caltech.
- ¹⁸Jacobson, S. A., and Reynolds, W. C., "Active control of streamwise vortices and streaks in boundary layers," *Journal of Fluid Mechanics*, 1998, **360**:179-211.
- ¹⁹Goldstein, D. B., Handler, R., and Sirovich, L., "Modeling a no-slip flow boundary with an external force field," *Journal of Computational Physics*, 1995, **105**:354-366.
- ²⁰Gad-el-Hak, M., "Interactive Control of Turbulent Boundary Layers: a Futuristic Overview," *AIAA Journal*, 1994, **32.9**:1753-1765.
- ²¹Lee, C. and Goldstein, D. B., "DNS of Microjets for Turbulent Boundary Layer Control," AIAA paper 2001-1013, 2001.
- ²²Lee, C. and Goldstein, D. B., "Simulation of MEMS Suction and Blowing for Turbulent Boundary Layer Control," AIAA paper 2002-2831, 2002.
- ²³Kim, J., Moin, P., and Moser, R., "Turbulence statistics in fully developed channel flow at low Reynolds number," *Journal of Fluid Mechanics*, 1987, **177**:133-166.
- ²⁴Lee, C. Y. and Goldstein, D. B., "Two-Dimensional Synthetic Jet Simulation," *AIAA Journal*, **40.3**:510-516.
- ²⁵Wu, K. E. and Breuer, K. S., "Dynamics of Synthetic Jet Actuator Arrays for Flow Control," AIAA paper 2003-4257, 2003.
- ²⁶Lee, C. Y., "Direct Numerical Simulation of Microjets for Turbulent Boundary Layer Control," Ph.D. Dissertation, Dept. of Aerospace Engineering, Univ. of Texas at Austin, Austin, TX., 2004.
- ²⁷Dahlburg, R. B., Sandberg, W. C., Handler, R. A., and Sirovich, L., "Direct numerical simulations of drag modifications using randomized force fields," Proceedings of the international symposium on seawater drag reduction, Newport, RI, July 22-23 1998, pp. 131-133.